



European Space Agency Contract Report

The work described in this report was done under ESA contract.
Responsibility for the contents resides in the author or organization that prepared it.

INFLUENCE OF THE TILT PARAMETER DURING SEE
CHARACTERIZATION WITH HEAVY ION BEAMS

FINAL REPORT

ESA Contract N° 13451/99/NL/MV
Ref. ESA_QCA 0317S_C

<u>Name</u>	<u>Function</u>
Prepared by: Guy Berger	Cyclotron Eng.
Denis Flandre	Professor, Head of DICE Laboratory.
Luis Moreno Hagelsieb	Researcher
Guido Ryckewaert	CRC Director
Reno Harboe Sorensen	ESTEC Technical Officer

December 2003

1. Introduction.....	3
1.1 Purpose of this document	3
1.2 Overview	3
2. Executive summary.....	5
3. Test structure process, simulations and in beam measurements	7
3.1 Test structures definition.....	7
3.1.1 Introduction	7
3.1.2 Technological simulations and process definitions	7
3.1.3 Mask layout and first clean-room fabrication	11
3.2 Test structures simulations.....	14
3.2.1 Time dependence	15
3.2.2 Ion track dependence	19
3.3 Test structures irradiations	27
3.3.1 Introduction	27
3.3.2 Pulse shape	27
3.3.3 Pulse amplitude discrimination	29
3.3.4 Multi Channel Analyzer	34
4. Complete structure simulations	37
4.1 Test structures definition.....	37
4.1.1 Introduction	37
4.1.2 Structure definition	37
4.2 Diode simulations.....	41
4.2.1 Ion impact localization influence.....	42
4.2.2 Ion strike time dependence.....	44
4.2.3 Reverse biasing influence.....	48
4.3 Transistor simulations	50
4.3.1 Well and ion strike localization influence.....	51
4.3.2 Well position and bias influences	55
4.3.3 Current dependency on ion track angle.....	57
5. Conclusions	66
APPENDIX 1. Input file for ATHENA and ATLAS	67
APPENDIX 2. Process sheets.....	69

1. Introduction

1.1 Purpose of this document

This document constitutes the “TILT Study” Final Report. It aims to correlate the influence of the irradiation parameters (tilted irradiations) on SEE characterization.

This work has been performed under ESA Contract N° 13451/99/NL/MV.

1.2 Overview

During Single Event Effect (SEE) characterization, beam parameters need to be modified to achieve a complete set of measurements. This implies to change the ion specie to modulate the amount of deposited charge in the sensitive volume. With ion changes, only a few data points can be taken. This lowers the sensitivity curve (cross section vs. Linear Energy Transfer LET) resolution and the users can easily miss some important parameters as the threshold LET for instance. A common method to increase the number of points on the cross section curve, and thus improve the characterization, is to use a tilt while irradiating. In this way, the ion path in the sensitive volume is increased and the generated charge can be modified. This method introduces the notion of effective LET (LET_{eff}). The LET_{eff} can be defined by the following expression:

$$LET_{eff} = \frac{LET}{\cos(\alpha)}$$

where α is the angle between the ion beam and the perpendicular to the device plane.

This method is widely used and generally gives good results. However, recent works have shown a strange behavior for some devices. Instead of a cross section increase for tilted devices, this one looks smaller. This phenomenon has been observed for digital as well as analog circuits, and is probably linked to a geometric effect. It is believed that if the device structure is vertical or horizontal, its behavior under tilted irradiation condition is different. A vertical structure will present a shorter ion track in the sensitive volume if tilted. This will lead to a lower generated charge in the sensitive volume and thus a smaller cross section value.

The goal of this work is to study this phenomenon. Correlations with simulations of test structures and in beam measurements helped to understand this strange behavior.

The first part of the report presents the chosen test structure and results obtained with it. Details are given on the technology and process. Simulations are presented for ion strikes at different angles and entry points. Experimental data are also presented and correlations with simulations are drawn.

In the second part of this report, a standard SRAM technology is presented. This one was the starting point for a more complete structure used for simulations. Here again, simulation results for normal and tilted conditions are given.

2. Executive summary

Since the unexpected SEE tilt effects were reported for components produced with recent IC processes, we focused our work on the charge collection in silicon devices with rather low junction depth and high substrate doping.

Simple PN test structures are best suited to determine the beam deposited charge under different test conditions and incident beam angles (i.e. tilt parameters). This data is required for reference and data correction purposes on actual device types.

For that purpose, a set of diode based test structures has been defined consisting in an array of diodes with different known topologies, i.e. areas, perimeters and junction depths, in order to allow a clear separation of the impacts in bottom and sidewall areas on the irradiation results.

Minimum dimension has been chosen equal to 6 μm , maximum equal to 100 μm and the junction depths equal to about 1 μm .

A number of technological simulations have been carried out with Silvaco ATHENA/ATLAS two-dimensional simulators, in order to optimise the simplest and most adequate complete process definition for our purpose. A complete set of simulations using ATLAS has been made for the 8 μm wide structure.

These simulations were performed for a 3V reverse bias. Entry points were modified in lateral coordinates as well as ion track angles. It is clearly shown that the current peak is much higher in the middle of the diode more than on the edge. Furthermore, for tilted irradiation conditions, the peak value decreases for increasing angle.

Simulation results for a normal incidence ion strike and zero bias for impacts starting in the middle of the diode ($X = 7 \mu\text{m}$) and shifted toward the edge show that the peak current amplitude is maximum and remains almost constant in the central part of the diode. Then decreases below half of the maximum value when the strike enters a peripheral zone at 2 μm from the edge, still shows an amplitude of about 20% of the maximum even at 2 μm beyond the device edge and finally shows a shifted time dependence as the strike leaves the device area.

Several simulations were also carried out for a constant tilted angle but for different entry points in the structure. It was observed that the peak cathode current was much higher for an ion strike in the middle of the structure than on the edge. For a 60° irradiation with entry points from left to right of the diode, the impacts present very different time characteristics. While tilted, the cathode current modification extends over a longer period of time when compared to a normal incidence impact. This may be linked to the fact that for normal incidence strikes, the pairs are generated in the same direction as the current

flow, and may have a faster contribution on the cathode current; whereas when the incidence is tilted, the pairs are created at remote locations from the device main electrical field and take more time to be collected.

The other consequence of the time characteristic shift is that the current peak value is lower for the tilted conditions than it is for a normal incidence.

Experimental data were obtained with a Xe 459 MeV beam provided by the Louvain la Neuve cyclotron and the Heavy Ion Irradiation Facility (HIF).

During irradiation, diodes were reverse biased at 3V and the collected charge was measured.

At normal incidence, most of the events occur for a collected charge of about 1 pC, which is in fair correlation with the charge computed using a 1D model and for an ion strike in the central part of the device. The number of occurrence for charges below half of the peak value accounts for less than 10 % of the total number of events, also in qualitative agreement with the area ratio, for a 100 μm x 100 μm device, between the central device zone and its peripheral zone starting at about 3 μm of the device edge, as observed in our simulations.

Furthermore, the collected charge amplitude also lowers with increasing angle while its distribution widens. It is also in fair agreement with simulations.

From simulations and experiments, we have demonstrated that the charge collection in PN diodes with CMOS-like low junction depth and high substrate doping decreases in amplitude and shows longer time constants when the ion strike is tilted or on the periphery of the device. We believe that these observations may intuitively explain the SEE cross-section decrease observed in recent components when tilted.

3. Test structure process, simulations and in beam measurements

3.1 Test structures definition

3.1.1 Introduction

During this study, the first step was to define a suitable test structure for simulation and in beam measurement. The proposed solution was a simple diode structure that can be processed in Microelectronics Laboratory (DICE).

Arrays of diodes with different geometries were realized. The different diodes have specific areas and junction depths.

According to DICE capabilities, minimum dimension can be chosen equal to 6 μm , maximum was chosen equal to 100 μm and different junction depths have been obtained varying the implantation energy on different processed wafers.

3.1.2 Technological simulations and process definitions

A number of technological simulations have been carried out to optimize the simplest and most adequate complete process definition for our purpose. Schematically, the process consists in the following steps:

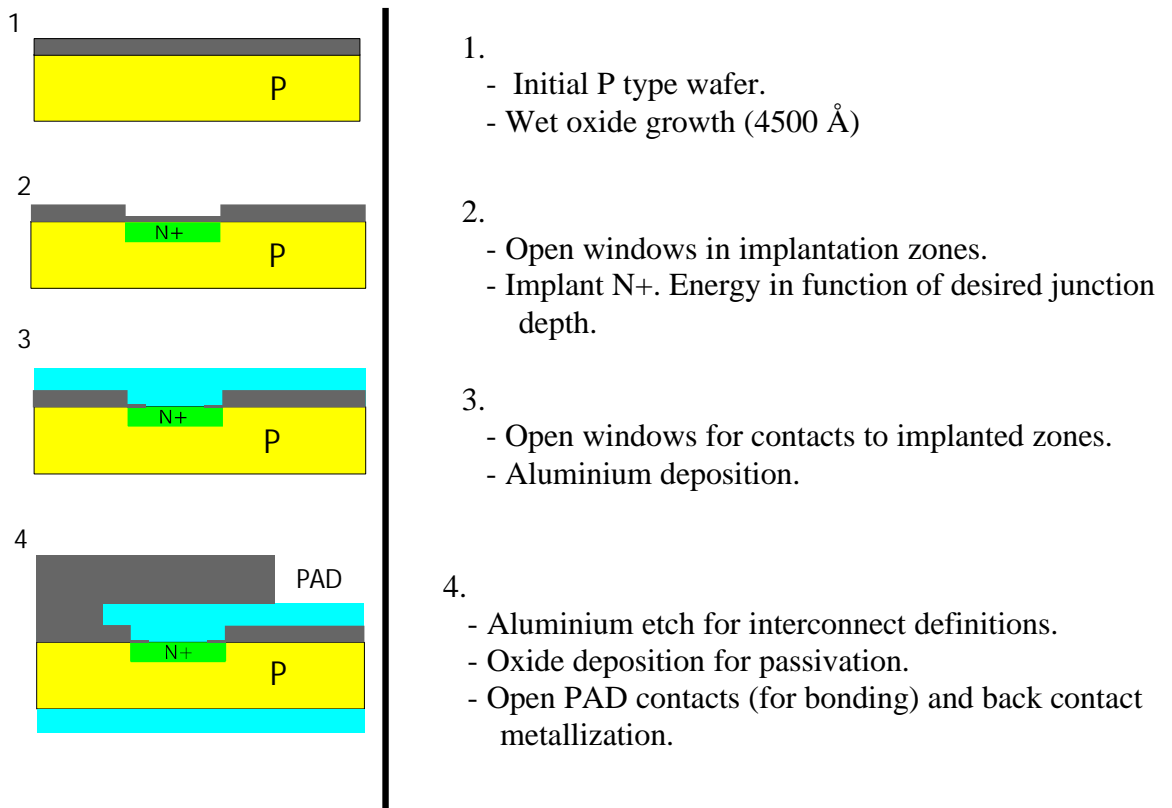


Figure 1. Simplified process flow

The energies of implantation have been adjusted by simulation to obtain three different junction depths according to the maximal and minimal energies of our machine, for a dose of 10^{15} cm^{-2} . The results are shown in table 1. Figure 2 shows the junction depth for the diodes implanted with the medium-level energy.

energy (KeV)	junction depth(μm)
180	1.45
100	1.1
20	0.75

Table 1. Junction depths for the energies selected (dose = 10^{15} cm^{-2})

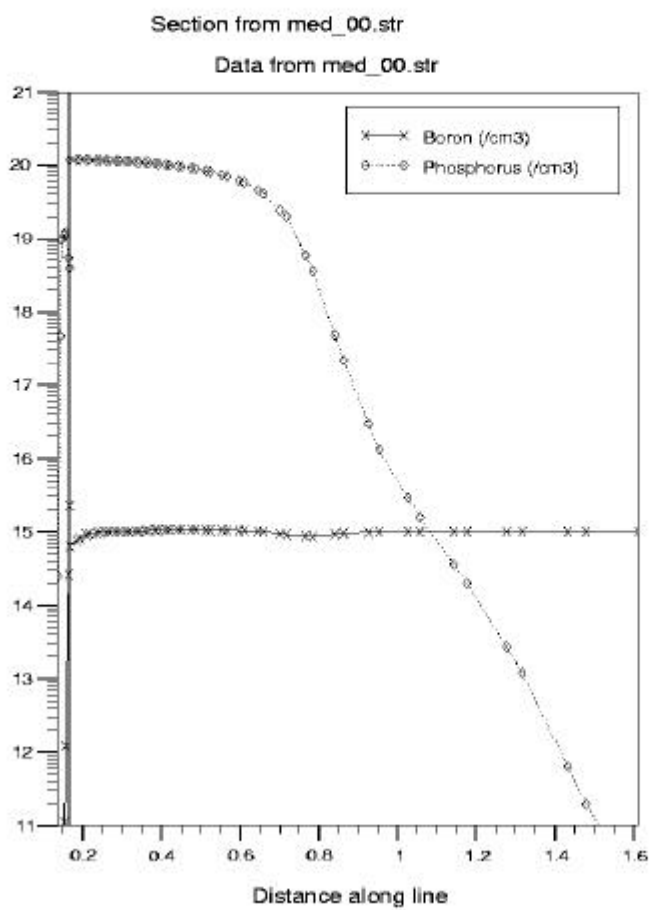


Figure 2. Depth junction for a 100 KeV implant energy

A final structure as obtained in ATHENA is shown in figure 3.

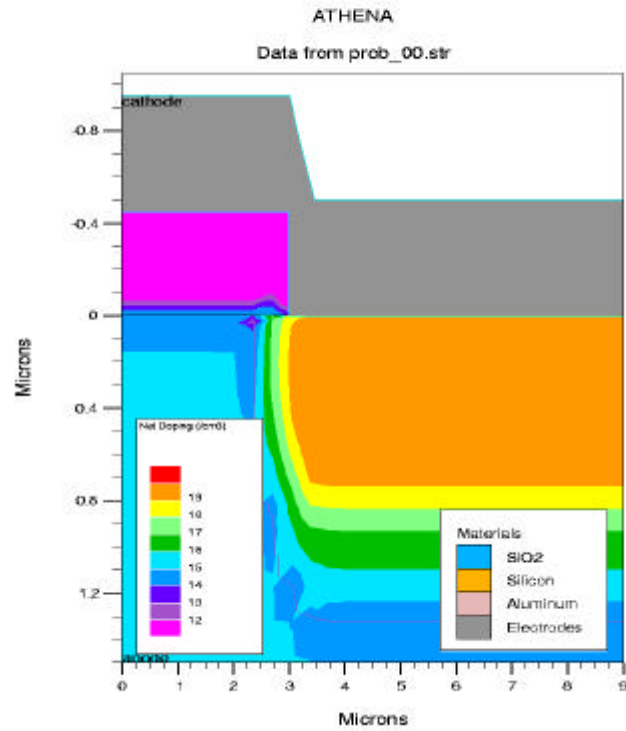


Figure 3. Structure generated by ATHENA

An example of an ATHENA file used for the process simulation is in appendix 1.

All the generated structures were finally simulated with ATLAS to obtain their DC current-voltage characteristics as is shown in figure 4 for one example.

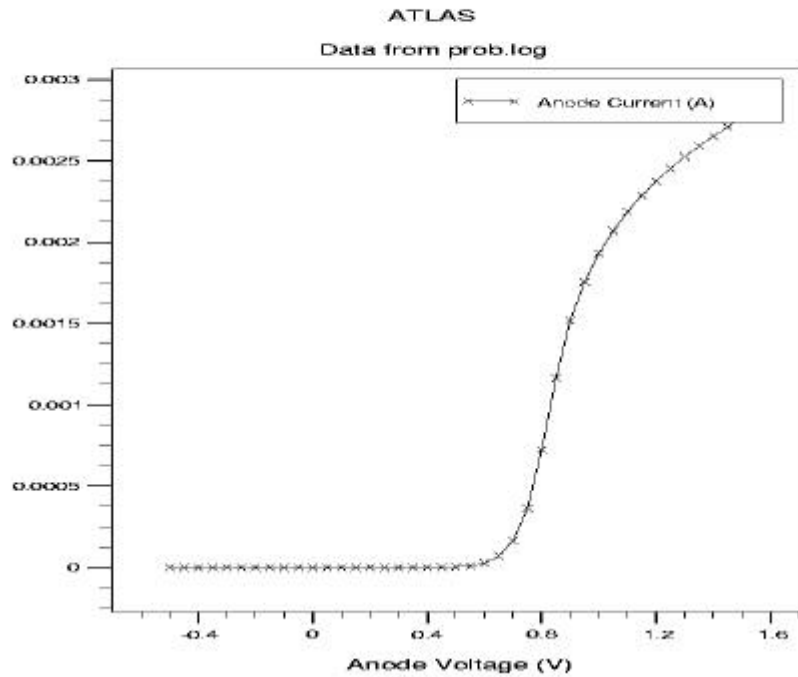


Figure 4. Diode current

3.1.3 Mask layout and first clean-room fabrication

The layout of the diode photolithographic masks has been designed on CADENCE. In order to obtain the dependence of charge recollection on the diode topological shape, the mask consists in an array of rectangular diodes with different lengths and widths as shown in figure 5 and Table 2. The distance between individual structures might also allow to record the effects of very large tilt angles on charge collection by neighbor structures and hence double upsets.

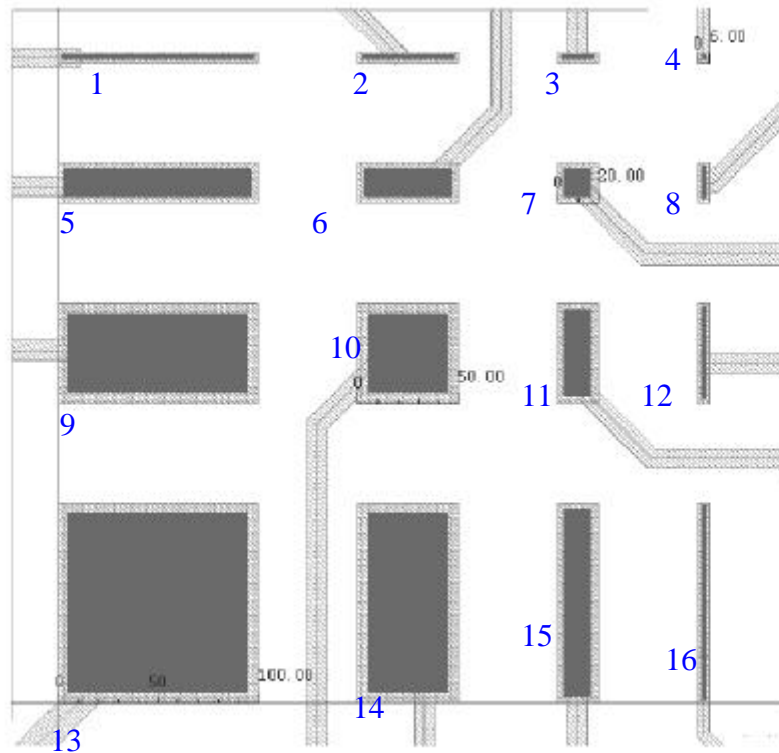


Figure 5. Layout of diodes

Some structures have been duplicated with different orientations to allow the study of orientation influence on charge collection. The exact dimensions of the 16 diodes in one array are given in table 2. Such arrays are repeated 49 times per wafer.

Diode number	Width	Length
1	100	6
2	50	6
3	20	6
4	6	6
5	100	20
6	50	20
7	20	20
8	6	20
9	100	50
10	50	50
11	20	50
12	6	50
13	100	100
14	50	100
15	20	100
16	6	100

Table 2. Diode sizes table.

Two wafers were implanted but a problem with the ion implanter stopped the process before the third implantation. We finished the process with only the two first implanted wafers (at 20 and 100 keV). Figure 6 shows photography of one of the arrays after fabrication.

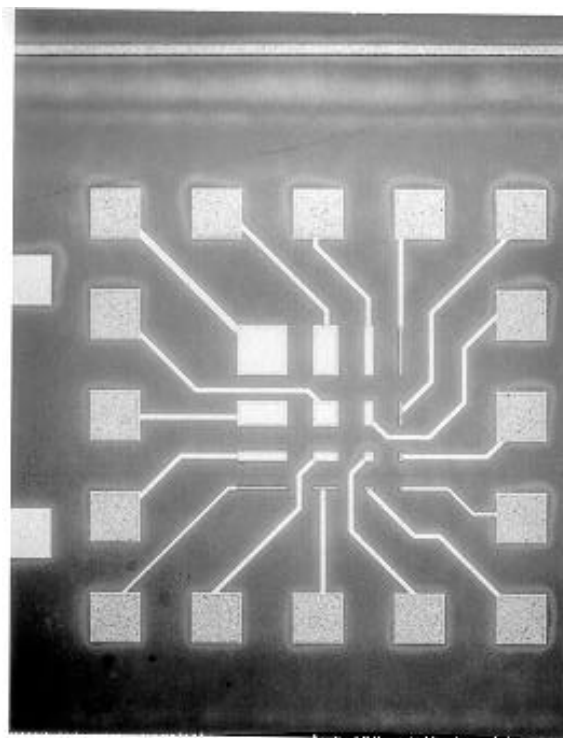


figure 6. Fabricated diode array photography.

3.2 Test structures simulations

Different simulations were carried out using ATLAS.

The figure 7 represents the simulated structure. This one is a $8\mu\text{m}$ geometry. This figure also represents the used meshing. As the region of interest is located in the middle of the structure, the horizontal meshing was made smaller in that region, while it was not necessary to refine it on the sides. The same assumption was made for the vertical meshing; the most interesting part is located on the upper part of the device. Meshing was refined on the top and enlarged in the bottom.

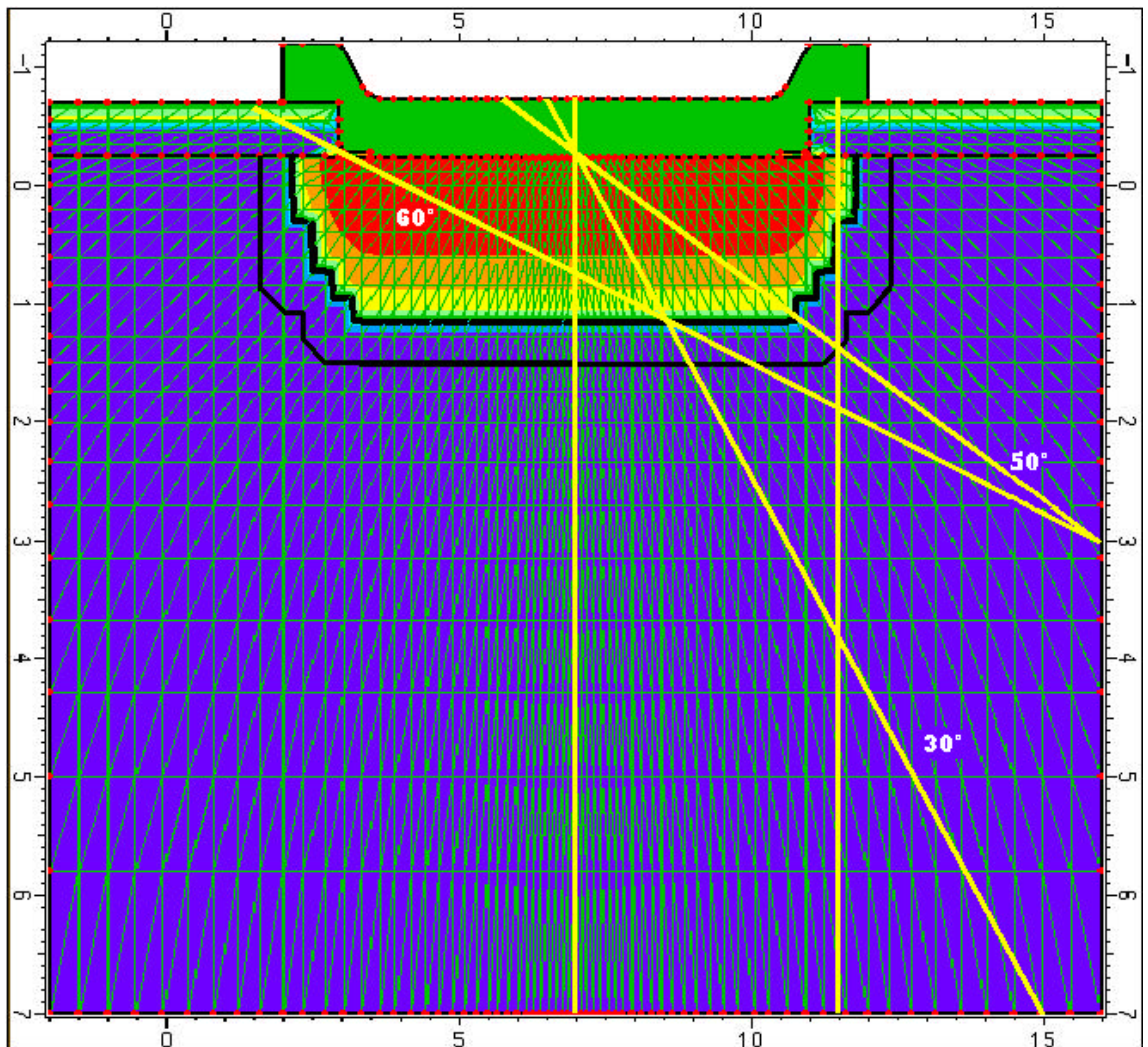


Figure 7: Structure meshing and ion tracks

As can be seen, ions strikes were done in the middle, on the edge and at three different angles (30°, 50° and 60°).

The charge generation was defined using the SINGLEEVENTUPSET statement of ATLAS. The statement allows specifying the entry and exit points as well as the beam parameters (deposited charge per ion track length unit [pC/μm]).

Simulations were done with Xenon ions at the same energy as used during experiment (459 MeV).

3.2.1 Time dependence

This first set of simulations was made to analyse the photocurrent time dependence of the ion strikes. Different T0 and TC values were used for this:

- T0 specifies the peak in time of the charge generation pulse.
- TC specifies the width of the charge generation pulse.

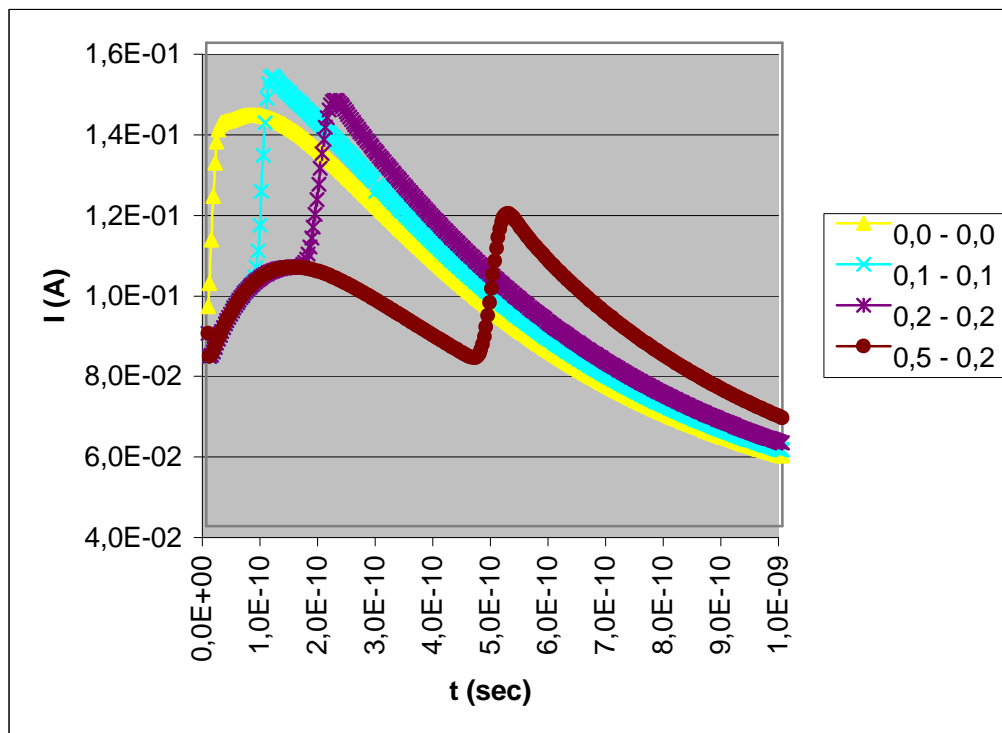


Figure 8: Single Event Upset responses of the current to T0 and TC variations

This figure shows how the influence starts at the time indicated by T0 and that when being in a higher IR area the effect is higher, T0 = 0,20 e⁻¹⁰ s and 0,50 e⁻¹⁰ s with same TC.

It is also clear how the simulation software considers an accumulated initial charge. For the last values, T0 = 0,5 e⁻¹⁰ s and TC = 0,2 e⁻¹⁰ s, two maxima can be observed, one from the initial charge and a second one coming from the SEU. In the three other simulations the peak is the result of the initial charge plus the SEU influence.

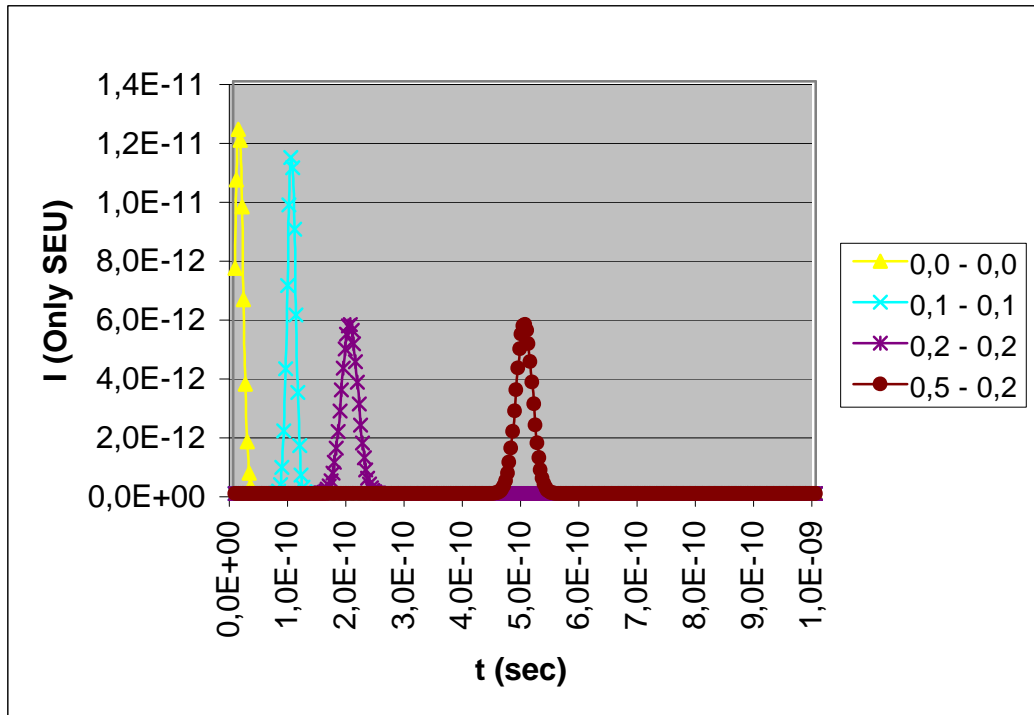


Figure 9: Single Event Upset photocurrent responses to T0 and TC variations

T0 and TC variations simulations. Only the induced photocurrent is plotted. T0 indicates the ion strike moment.

We see that TC variations produce different peak values. For the same pulse width (data set 3 and 4 in fig. 9) peak values are the same while lowering TC induces higher peak currents.

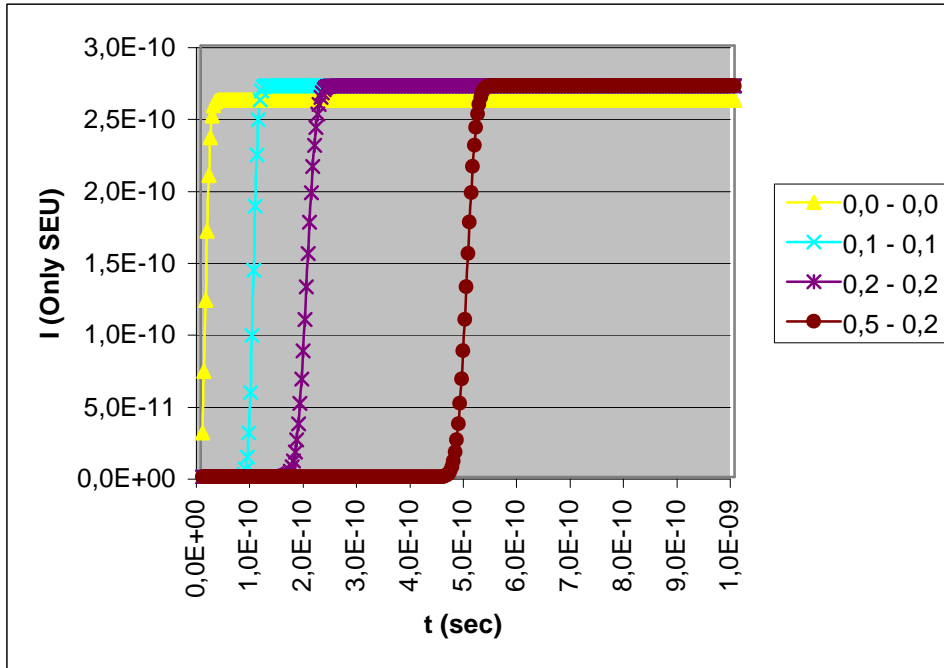


Figure 10: Single Event Upset photocurrent responses to T0 and TC variations

T0 and TC influence on the cumulative SEU photocurrent. TC affects the time to reach the current upper limit. For T0 = 0, the upper limit is lower than in the other cases.

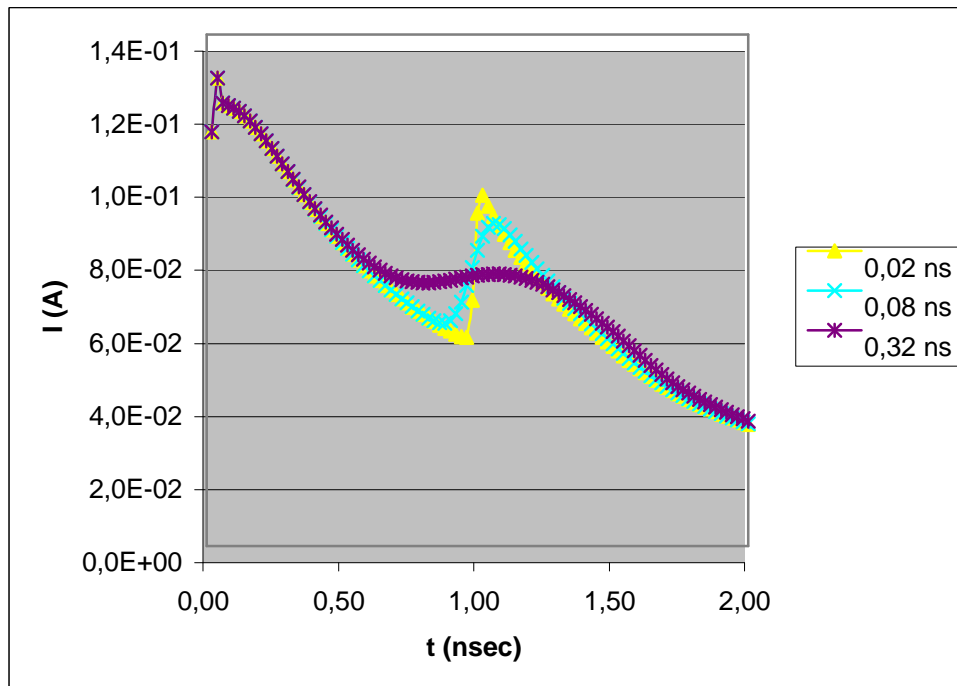


Figure 11: cathode current response to TC variation

Simulation of the cathode current for a $T_0 = 1e^{-9}$ s and three different values for TC (0,02 – 0,08 and 0,32 ns). Higher values of TC induce a lower current, but the effect extends on a longer time.

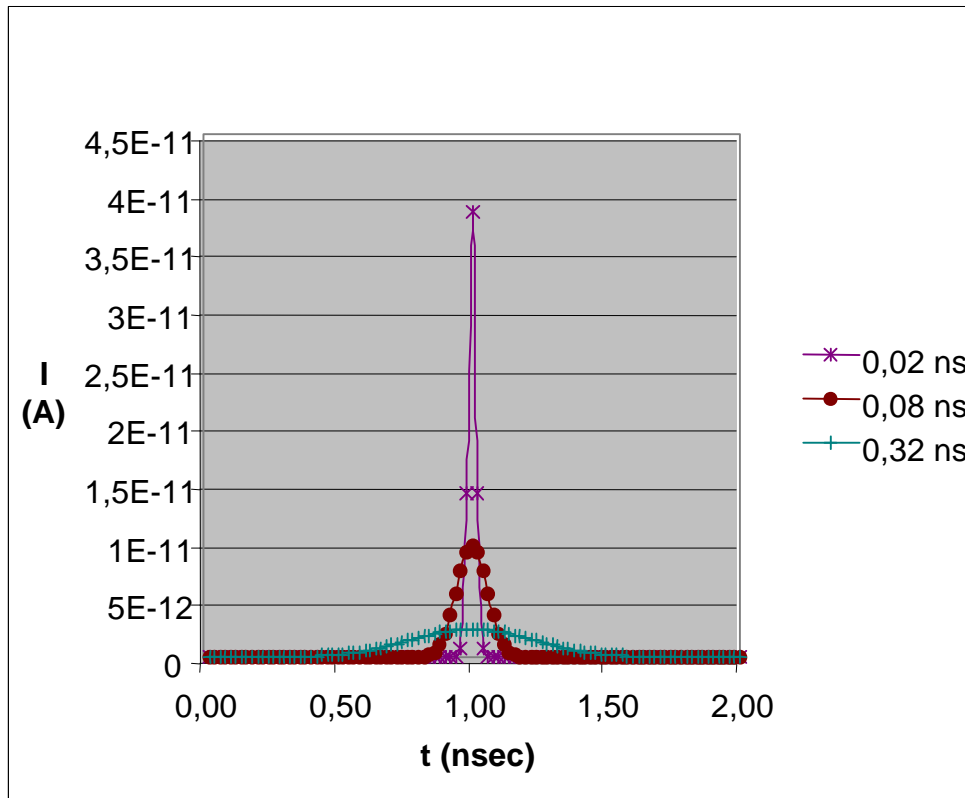


Figure 12: photocurrent response to TC variation

The same simulation as above, but only the photocurrent value is plotted. Here again we see that the maximal value of the photocurrent is larger for short TC, and that the phenomenon extends on a larger period of time for low TC values. Another point is that the integrals of each peak are the same; there is no influence of TC value on the peak area.

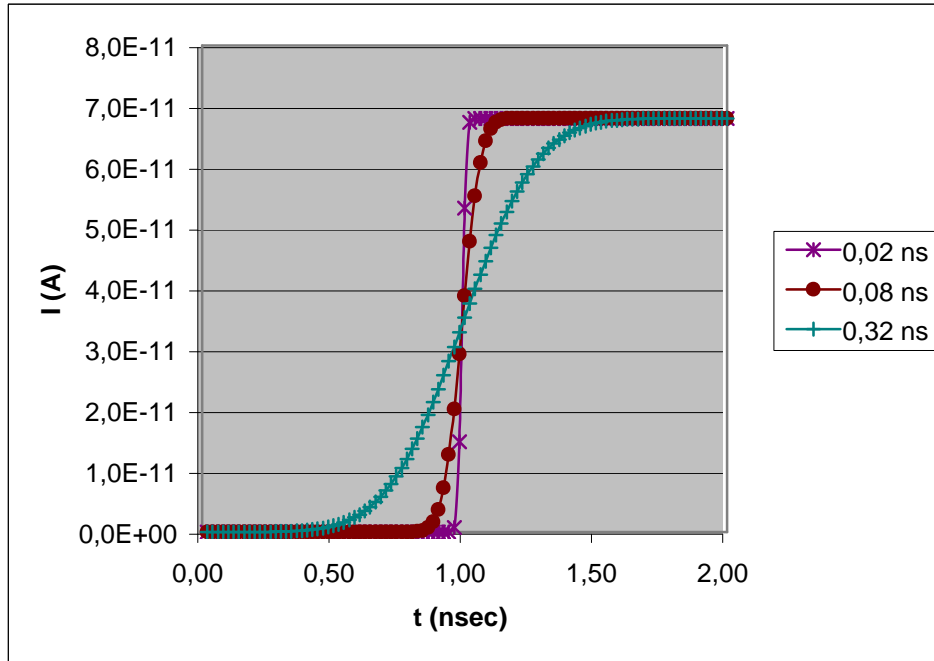


Figure 13: cumulative photocurrent response to TC variation

Same simulation showing the cumulative photocurrent. As expressed above, the upper limit is the same for the three TC values. This limit is reached faster for short TC.

3.2.2 Ion track dependence

In the second set of simulations, T_0 and TC were kept constant, but ion entry and exit points were modified. These simulations present results for one particular angle and for different entry points. Two angles have been selected: 0° (labelled 90) and 60° . For each plot, data are presented using two coordinates, the first is the angle and the second one is the entry point coordinate in μm (cf. figure 7 showing the meshing).

Entry points for normal incidence strikes start in the middle of the structure (90-7) and end outside of the diode (90-14). For the tilted irradiations, entry points start on the left side and outside of the diode (60-0) and end on the diode edge (60-10).

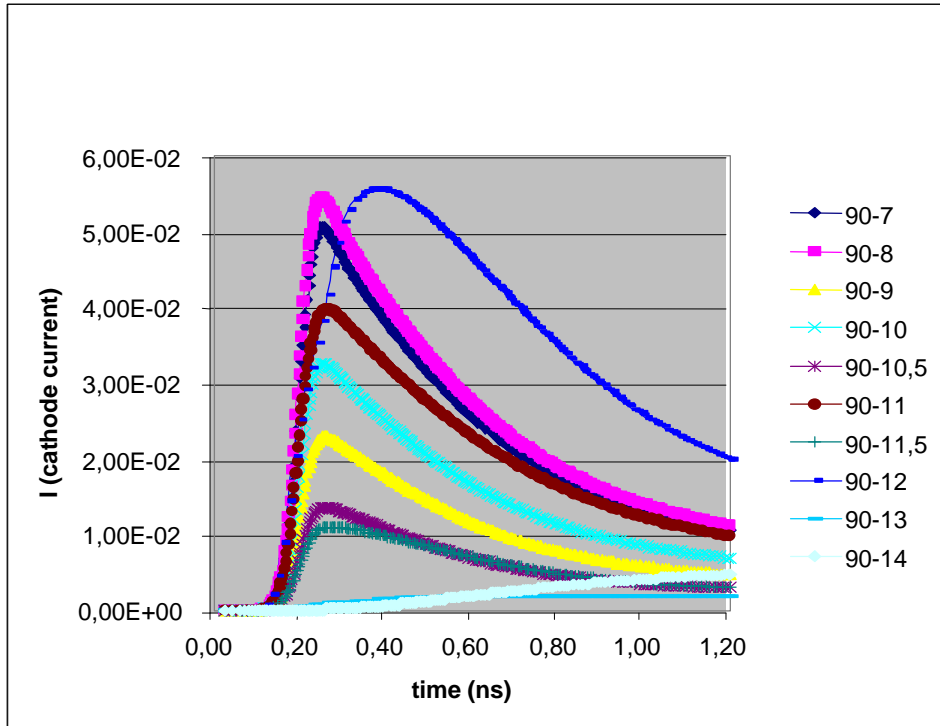


Figure 14: SEU simulation positional influence for normal incidence

Here we see the positional influence of the ion strike on the total current. The highest current values correspond to ion strikes in the middle of the structure (90-7, 90-8) and on its edge (90-12).

The possible reason that the current is larger on the edge is that the ions pass through a higher depletion region on the edge and created charges reach faster the electrodes.

As expected, outside the diode (position 13 and 14) we observe a minimal effect.

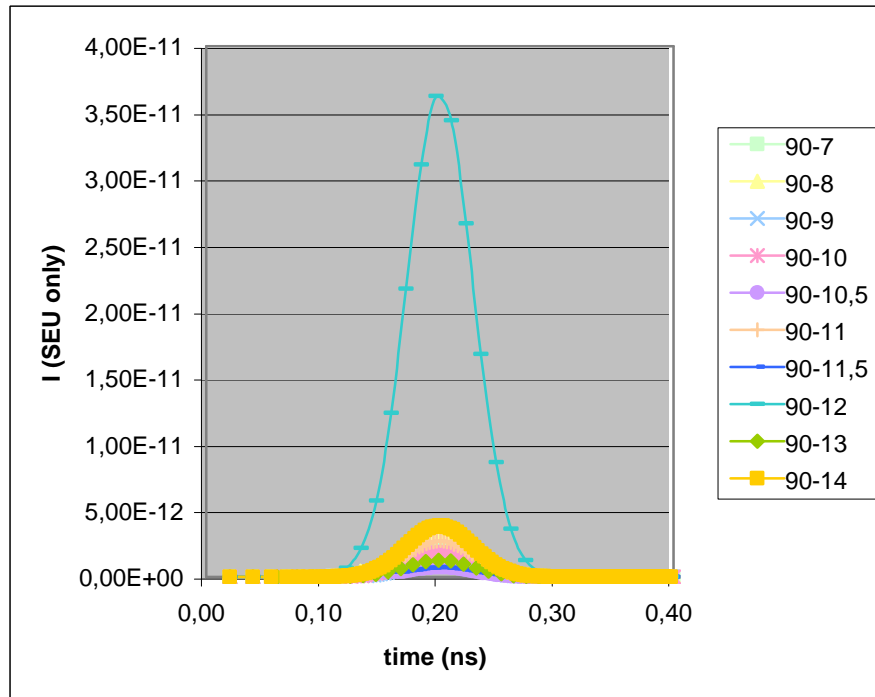


Figure 15: SEU simulation positional influence for normal incidence

This figure represents the temporal distribution of the photocurrent. It is clear that when the ion strike is located on the diode edge (90-12), the current peak value is much higher than in any other case. This confirms that when the ions reach higher depletion regions the global effect is increased.

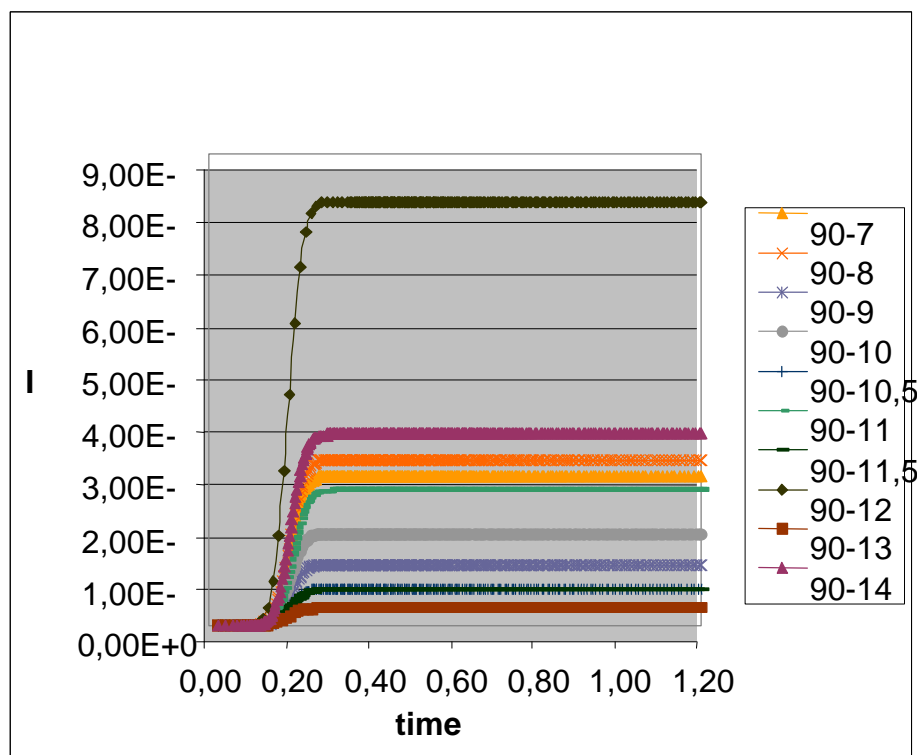


Figure 16: SEU simulation positional influence for normal incidence

Same simulations as above showing the cumulative photocurrent. As expressed above, the total current is much higher for edge strikes (90-12).

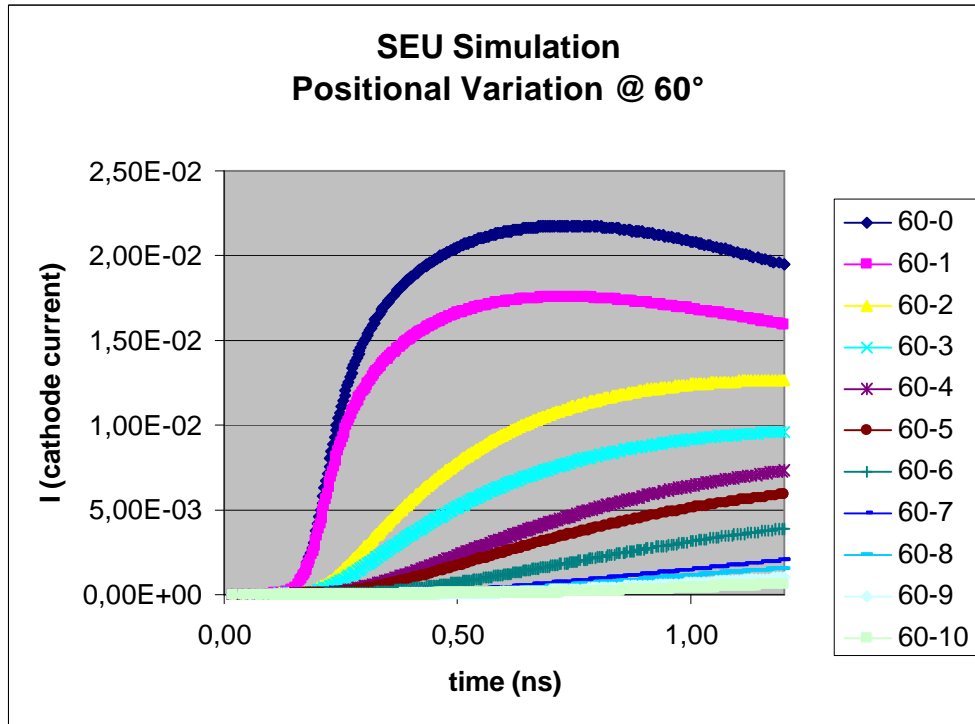


Figure 17: SEU simulation positional influence for tilted irradiation

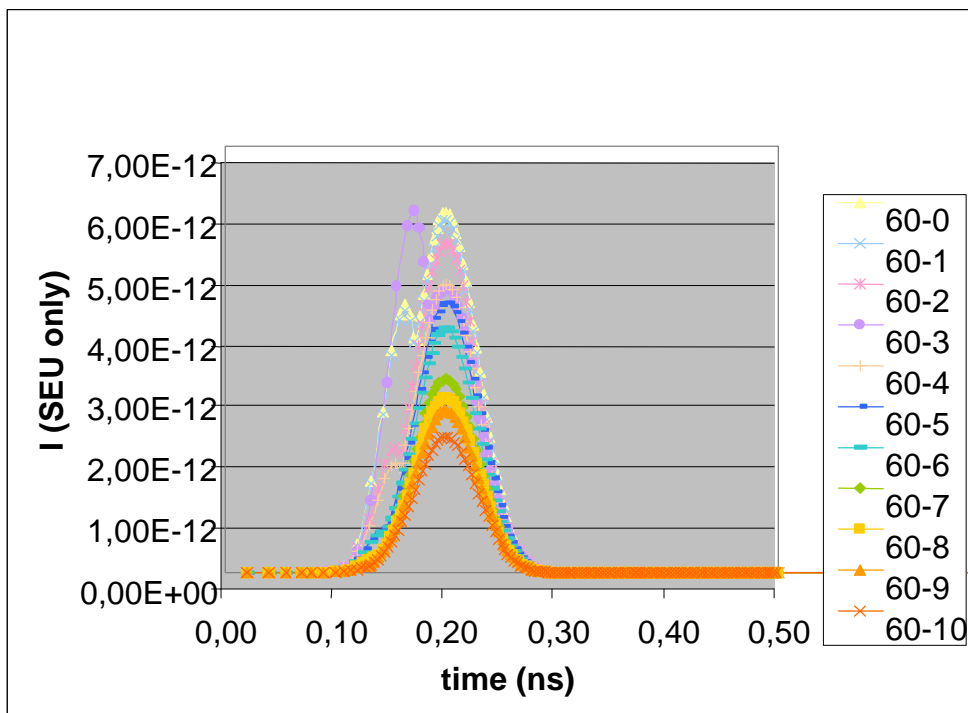


Figure 18: SEU simulation positional influence for tilted irradiation

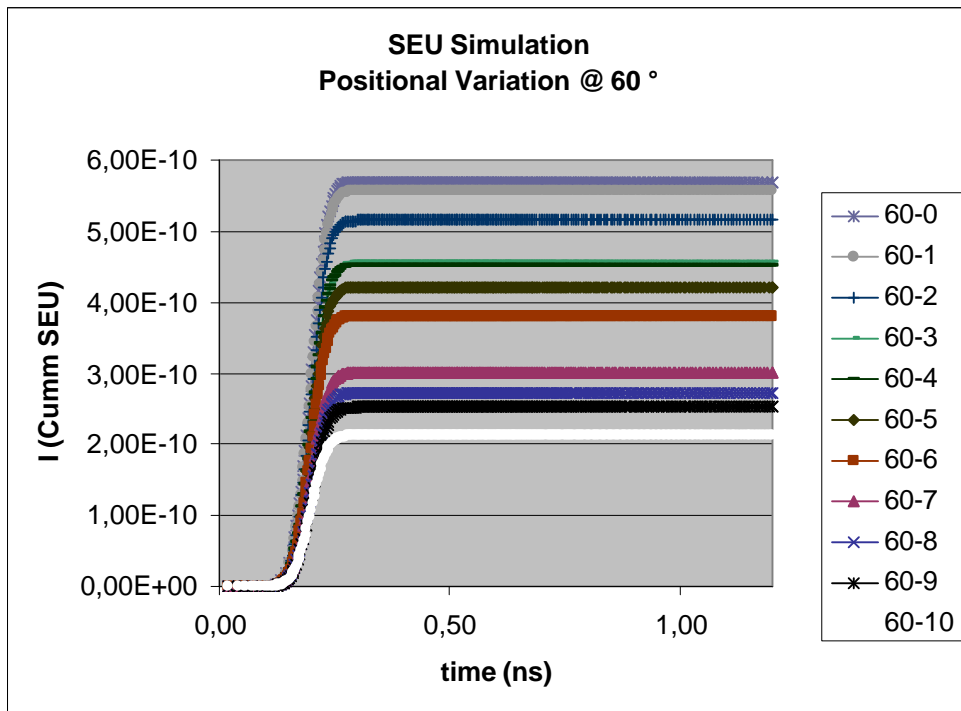


Figure 19: SEU simulation positional influence for tilted irradiation

For tilted irradiation, we see that when the ions pass through a larger diode area, the total current value is higher. This is because the ion tracks reach more depletion region.

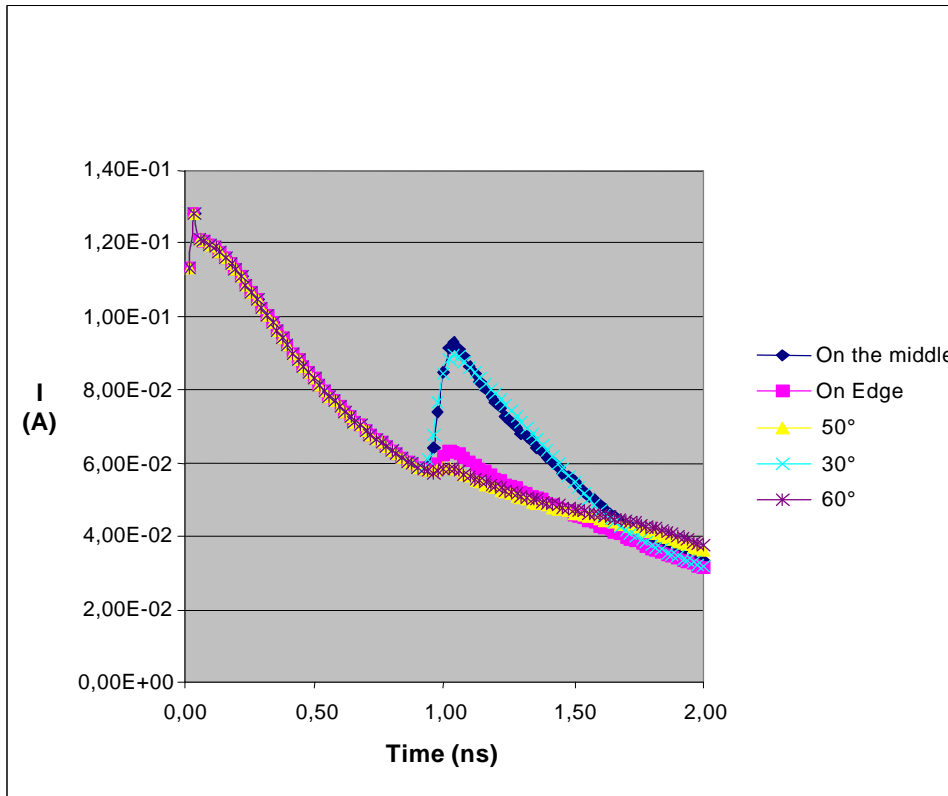


Figure 20: SEU simulation angular and positional influences

These simulations give SEU results for two normal incidence ion strikes and for three angles. Normal incidence irradiations were performed in the middle of the structure and on the edge (just at the beginning of the oxide area). As can be observed, middle strike induces a larger current than a lateral one. For the tilted strikes, hit at 30° and 50° had entry points at the middle of the structure, while for the 60° irradiation, the entry point was located on the left side of the structure. We can observe that the smallest angle produces the larger current.

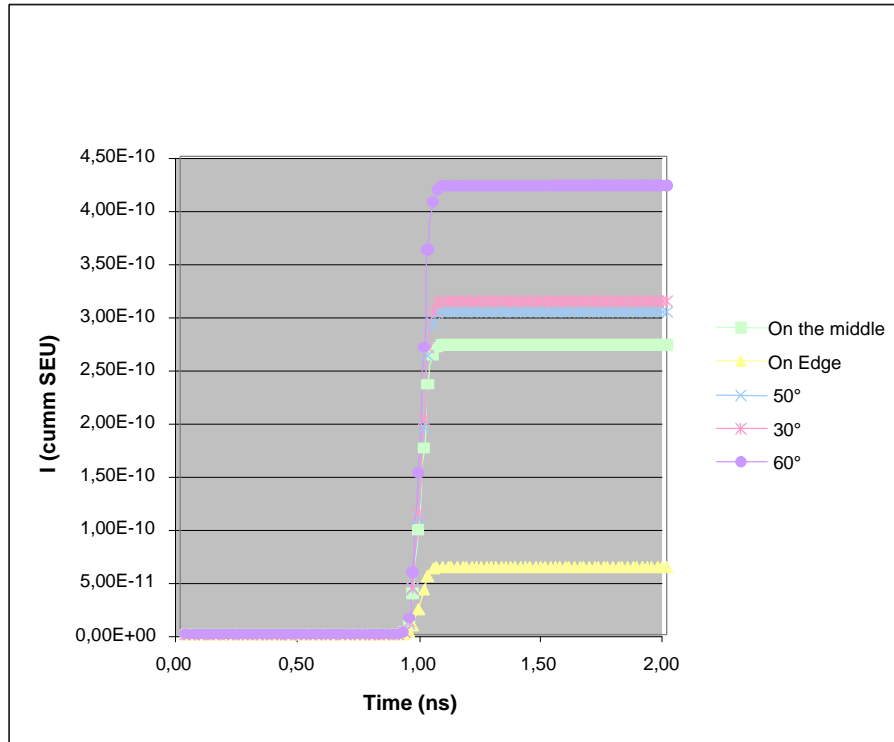


Figure 21: SEU simulation angular and positional influences

Same simulations as above showing the cumulative photocurrent. It can be seen that the needed time to reach the maximal current is very similar in each case, but the maximal current levels are different. We see that the larger the angle is, the larger the cumulative photocurrent is. This can be explained as the ion track covers a larger depletion region.

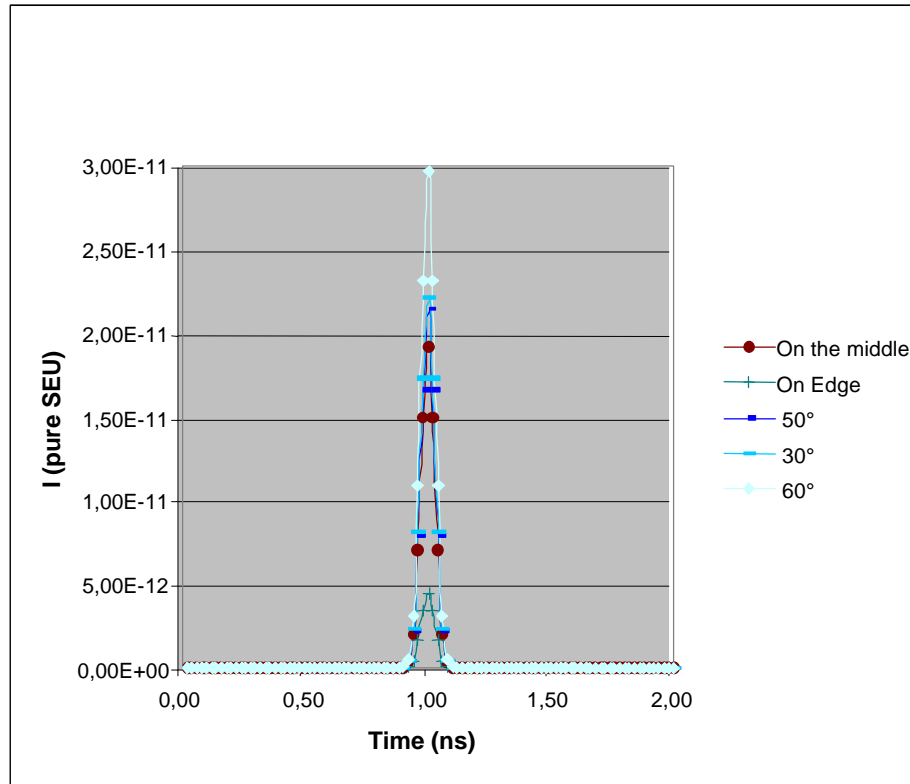


Figure 22: SEU simulation angular and positional influences

This plot represents the temporal distribution of the photocurrent. This confirms the previous conclusion: the higher the ion strike angle is, the higher the photocurrent peak is. If we now compare this with the figure 20, we see that even if this photocurrent peak value is higher for large angles, the total cathode current is lower. This can be explained by the fact that in this case, the created charges take more time to reach the electrode. The collecting phenomenon is spread on a larger period of time.

3.3 Test structures irradiations

3.3.1 Introduction

Several test campaigns have been carried out on these test structures. During some of the test periods, emphasis was placed on the outgoing signal shape during irradiation. Signal was then chopped and a complete pulse height analysis was carried out. Two different methods were used for this latter purpose: Constant Fraction Discriminator (CFD) and Multi Channel Analyzer (MCA). All irradiations were carried out using a Xenon beam at a total energy of 459 MeV provided by the Louvain la Neuve cyclotron and the Heavy Ion irradiation Facility. During irradiation, diodes were reverse biased at 3V

3.3.2 Pulse shape

Two different structures have been irradiated, the 100 X 100 μm and the 50 X 50 μm . The largest one was irradiated at 0 and 60 ° to see the angle effect on the pulse distribution.

The diode signal was fed in a charge preamplifier. It's output was then injected in a spectroscopy amplifier to have a sufficient pulse height.

Used equipment:

- Preamplifier CANBERRA model 2004.
- Amplifier CANBERRA model 2012.

After a first evaluation, it was clear that the output signals present a large spread in amplitude; it was then needed to do an envelope acquisition in order to point this out. For each irradiation, a total of 100 acquisitions were added in the envelope mode. The results of the most significant runs are represented hereafter.

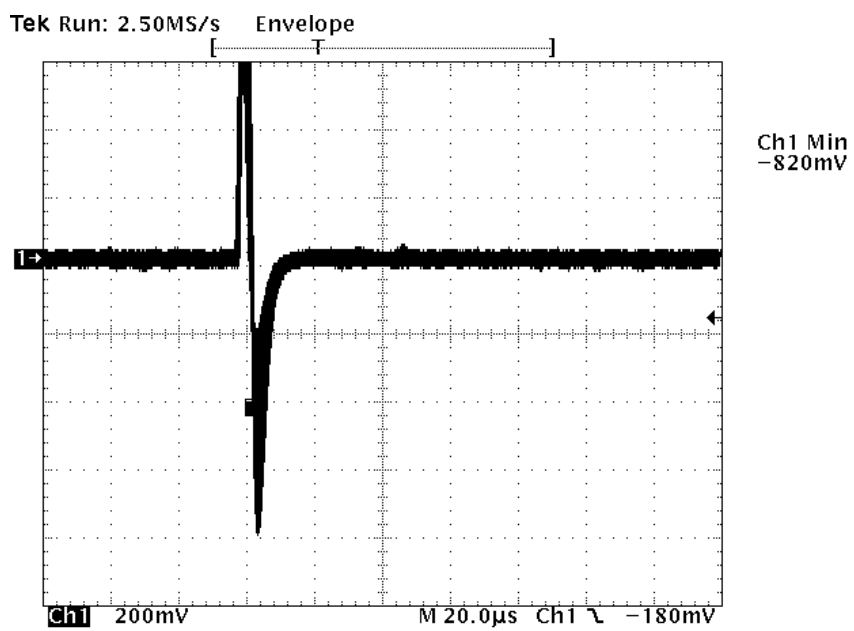


figure 23: 100 X 100 µm diode, Xe beam at 0°.

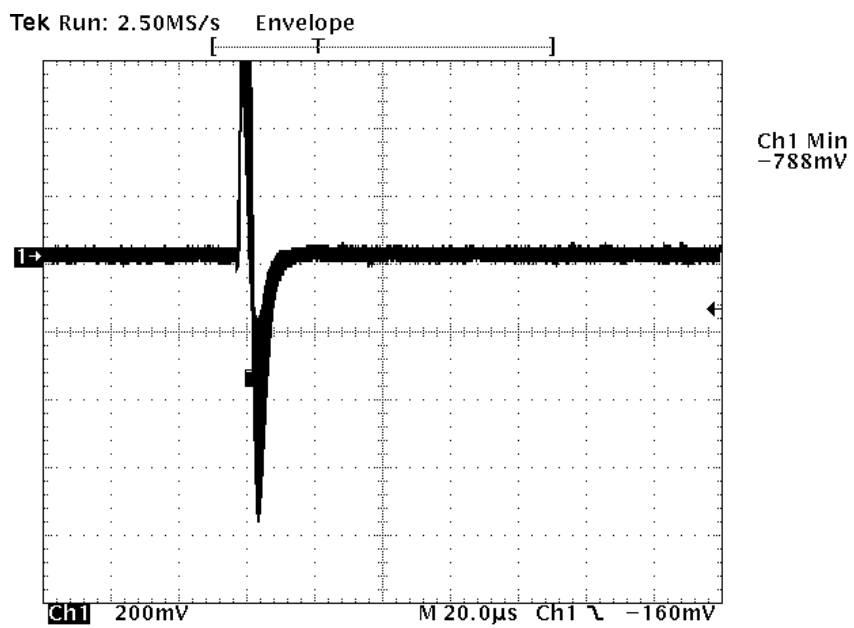


figure 24: 100 X 100 µm diode, Xe beam at 60°.

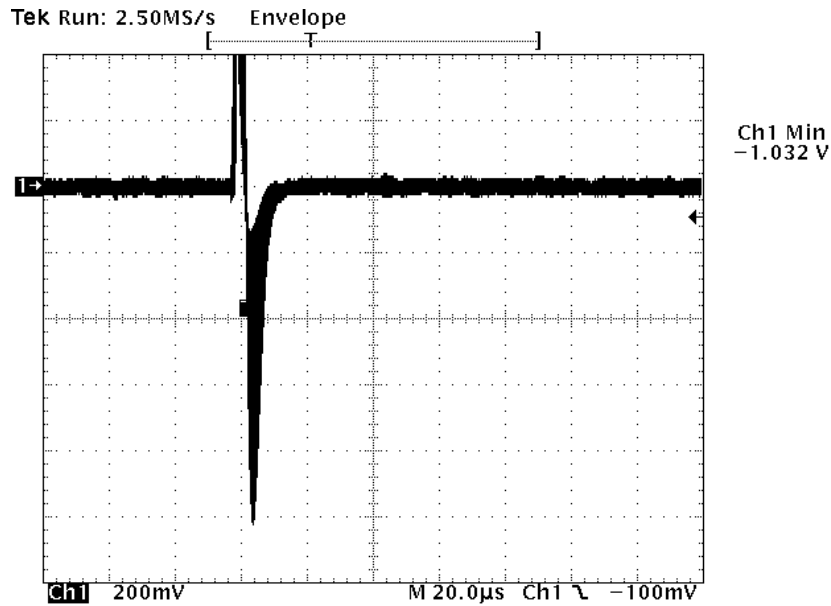


Figure 25: 50 X 50 μm diode, Xe beam at 0° .

A straight comparison of these screen shots shows that the output signal amplitudes are distributed as follows:

Diode size - beam	Min amplitude	Max amplitude
100 X 100 μm – Xe 0°	200 mV	820 mV
100 X 100 μm – Xe 60°	200 mV	788 mV
50 X 50 μm – Xe 0°	150 mV	1.03 V

Table 3: Signal amplitudes.

It looks like for the same diode, while tilted, the maximal amplitude of the signal is lower than at normal incidence. This phenomenon was observed during later irradiations. This will be detailed later in the report.

The second observed effect is the large difference in the signal maximal amplitude for the smaller diode size. This could be understood as a strong perimeter – area ratio dependency of the structure (the smaller feature size has the larger ratio). This will also be pointed out later in the report.

3.3.3 Pulse amplitude discrimination

The next step was to use a constant fraction discriminator to have an amplitude histogram. This was done using the same setup as before, but adding octal Constant Fraction Discriminators (CFD) in the line. Thresholds for each CFD were set to reach 50 mV channel width (Bin).

The counting rate for each bin was then normalized by the total fluence to obtain a value labeled Sigma. In addition, all three distributions were normalized to the same beam fluence. This was necessary because the 100 X 100 μm structure irradiated at 0° received $2.4 \text{ E6 ions/s cm}^2$ while the two other irradiations were performed at $1.5 \text{ E6 ions/s cm}^2$.

The following tables and figures give the distributions for each irradiation.

CFD Bin	Sigma
1	8,29E-07
2	1,66E-06
3	2,49E-06
4	0
5	2,9E-06
6	3,73E-06
7	4,97E-06
8	5,68E-05
9	5,63E-05
10	3,48E-05
11	0
12	5,39E-06
13	4,55E-06
14	8,28E-07

Table 4: 100 X 100 μm diode irradiated at 0° .

CFD Bin	Sigma
1	3,67E-05
2	7,66E-05
3	1,60E-05
4	2,67E-06
5	4,67E-06
6	1,87E-05
7	9,53E-05
8	4,20E-05
9	3,60E-05
10	1,33E-05
11	2,00E-06
12	0,00E+00
13	0,00E+00
14	0,00E+00

Table 5: 100 X 100 μm diode irradiated at 60° .

CFD Bin	Sigma
1	9,99E-06
2	2,66E-06
3	7,99E-06
4	9,32E-06
5	3,99E-06
6	6,65E-06
7	7,32E-06
8	1,86E-05
9	3,78E-05
10	3,91E-05
11	2,32E-05
12	7,96E-06
13	9,32E-06
14	1,4E-05

Table 6: 50 X 50 μm diode irradiated at 0°.

After the irradiation, the response of the system was calibrated by using a pulse generator (ORTEC model 448) together with its associated charge terminator to inject a known quantity of charge into the detector input of the preamplifier. In this way, it is possible to estimate the quantity of collected charge from the positions in the histograms.

In Preamp [mV]	OUT Amp [mV]	Q [pC]
-100	-388	1,30
-125	-484	1,50
-150	-580	1,71
-175	-696	1,95
-200	-776	2,11
-250	-892	2,36

Table 7: Amplifier charge calibration.

This gives us the following calibration:

CFD Bin	Q [pC]
1	0,06
2	0,18
3	0,29
4	0,41
5	0,52
6	0,64
7	0,76
8	0,87
9	0,99
10	1,10
11	1,22
12	1,33
13	1,45
14	1,57

Table 8: CFD calibration.

The different histograms have been normalized to give the collected charge distributions:

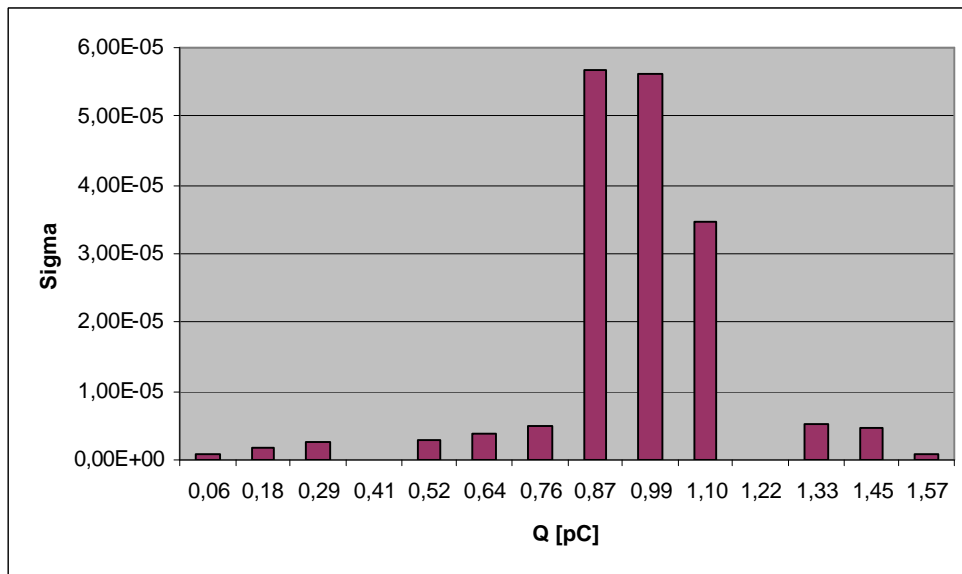


Figure 26: 100 X 100 μm diode irradiated at 0°.

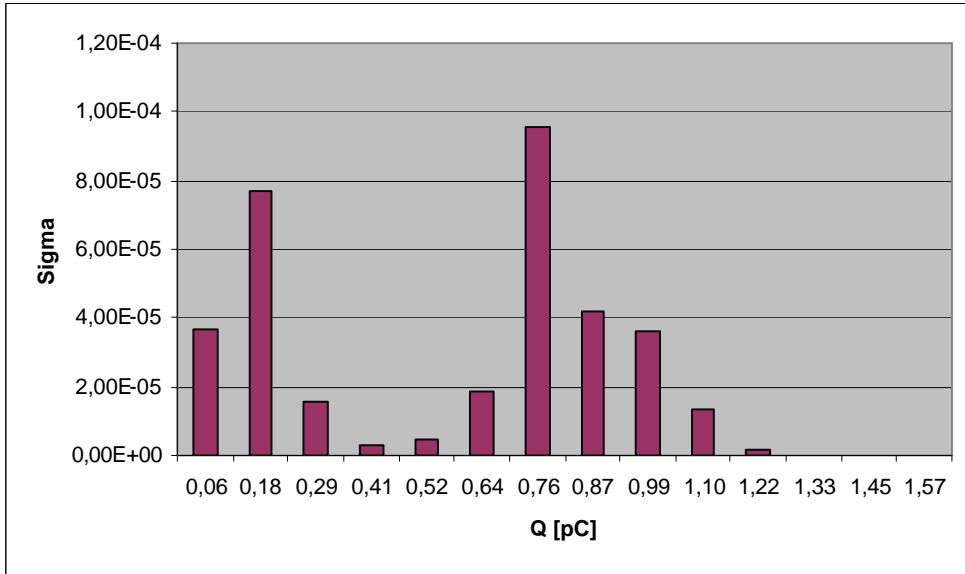


Figure 27: 100 X 100 μm diode irradiated at 60° .

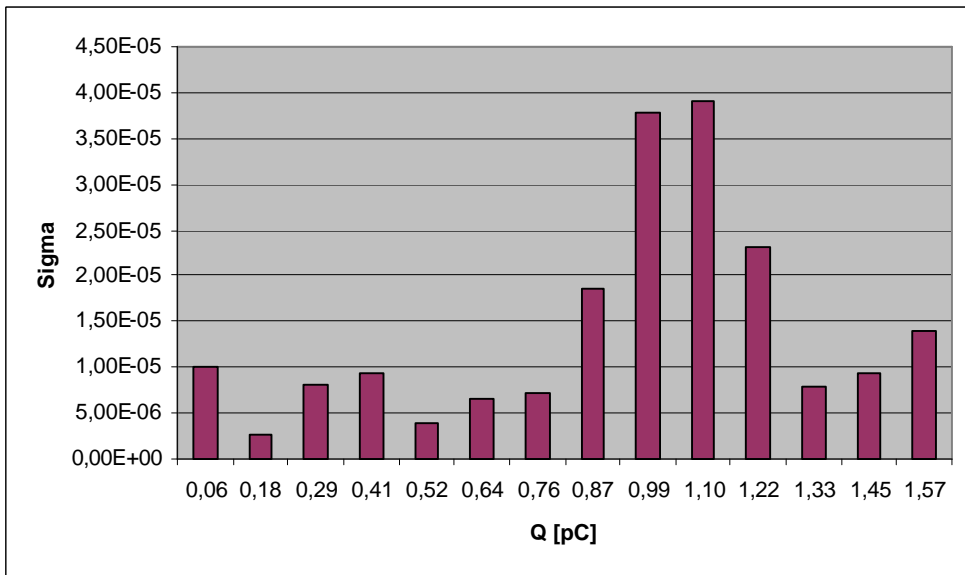


Figure 28: 50 X 50 μm diode irradiated at 0° .

The tilted diode presents a smaller charge than the un-tilted one. For 60° irradiations, the distribution centroid is around 0.8 pC while for normal incidence irradiations, it is 1 pC.

We can also observe that for tilted irradiations, the distribution is quite different than the zero degree. The data are not more centered on a certain value, but we observe a double peak structure. A second distribution is present at lower charge values (0.18 pC).

It is also clear that for normal incidence irradiations for two diode feature sizes, the smaller size shows the larger collected charge (up to 1.5 pC). This can be explained by the perimeter – area ratio.

The perimeter – area ratios for both structures are $4 \cdot 10^{-2} \mu\text{m}^{-1}$ for the 100 μm structure, and $8 \cdot 10^{-2} \mu\text{m}^{-1}$ for the 50 μm structure. The fact that this ratio is larger for smaller feature size has to be correlated with what has been explained before (fig. 14). Ion hits on the edges of the structure produce larger currents than centered strikes.

3.3.4 Multi Channel Analyzer

During this test period, the diode was connected via the charge preamplifier and spectroscopy amplifier (same as above) to the MCA. The gain of the amplifier was adjusted so that we observed a good signal – noise separation. The MCA was used to measure the mean pulse height (peak centroid) of the signal output of the amplifier.

After the irradiation, the response of the system was calibrated by using the same procedure as for the CFD. In this way, it is possible to estimate the quantity of collected charge from the positions of the MCA peaks.

On the figure 29, 2 sets of data are shown. These spectra are taken for the 100 X 100 μm diode, reverse biased at 3 V for two different irradiation angles. The green line represent the data set for the normal incidence, while the red spectra is for the 60° irradiation.

The figure 30 represents the calibration spectra, every peak represent a specific deposited charge. The peak position determination was made using the MCA software (from AMPTEK), the resulting file is presented in table 9. Table 10 gives the deposited charge for each peak position.

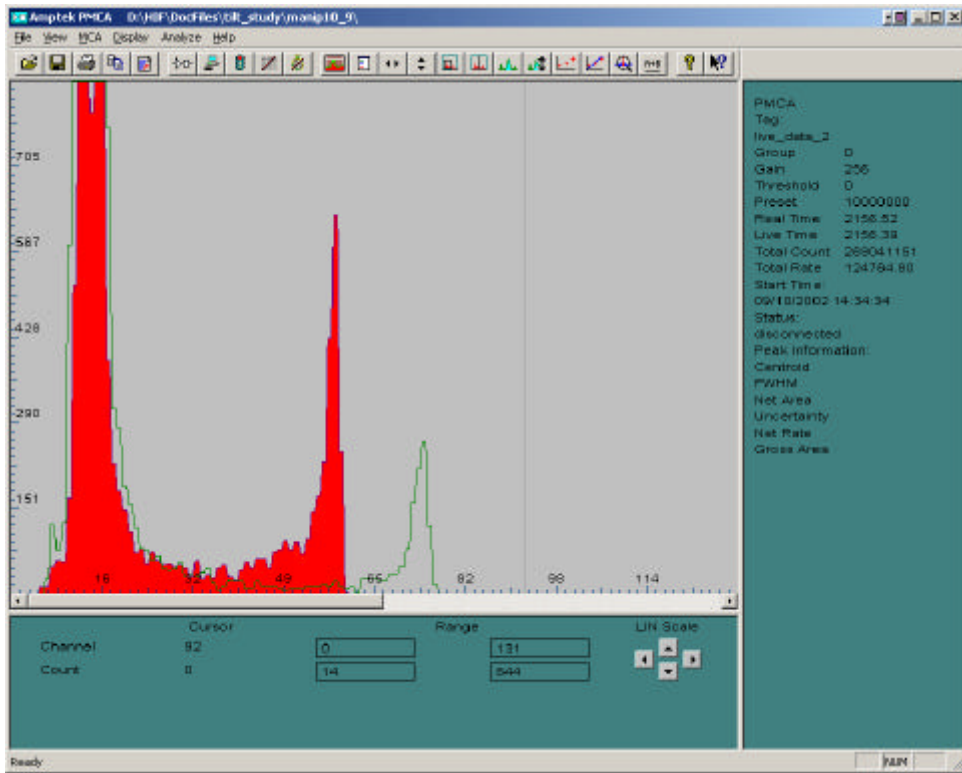


Figure 29: 100 X 100 μm diode irradiated at 0° and 60°

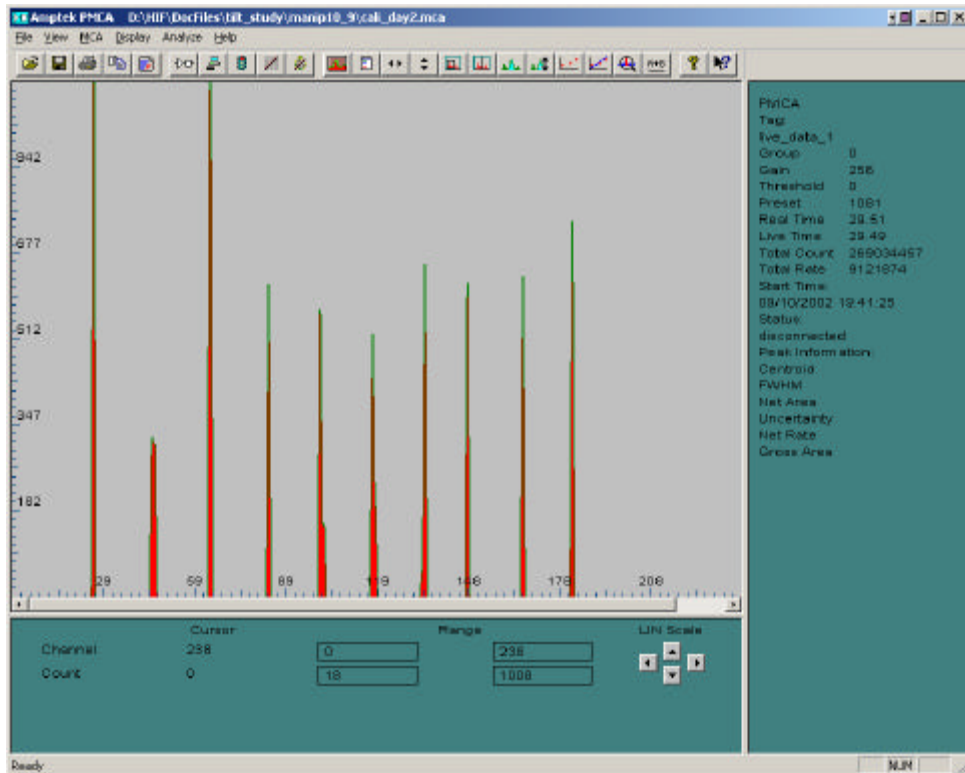


Figure 30: MCA calibration.

Start	End	FWHM	Net Area	Gross Area	Centroid	Uncertainty	Status
19	33	1.000	1442	1442	26	2.63	GOOD
39	52	1.977	634	634	45.49	3.97	GOOD
57	71	1.000	1757	1757	64	2.39	GOOD
76	89	1.011	632	632	82.98	3.98	GOOD
94	107	1.193	730	730	100.22	3.70	GOOD
111	124	1.292	717	717	117.27	3.73	GOOD
127	141	1.057	724	724	133.91	3.72	GOOD
141	155	1.000	622	622	148	4.01	GOOD
159	173	1.000	634	634	166	3.97	GOOD
175	189	1.000	741	741	182	3.67	GOOD

Table 9: Calibration peak detection.

Peak channel	Q [pC]
26	0.5
45	0.7
64	0.9
83	1.1
100	1.3
117	1.4
134	1.6
148	1.7
166	1.9
182	2.1

Table 10: Peak to charge calibration.

Using a linear regression method, a calibration formula was calculated to give us the collected charge in function of the peak position:

$$Q [pC] = 0.01 * Channel + 0.25$$

Having this MCA calibration, we can observe that the obtained data using the CFD technique are exactly the same as with the MCA. Same conclusions can be drawn. The collected charge for untilted diode is larger than for the tilted one.

Peak channel	Q [pC]
70	0.95
53	0.78

Table 11: Collected charge for the 100 X 100 μm diode.

4. Complete structure simulations

4.1 Test structures definition

4.1.1 Introduction

The next step in this project was to simulate a more detailed structure, and see if previous conclusions can be extrapolated to this one.

We tried to simulate a structure that was used in a standard SRAM technology.

4.1.2 Structure definition

We based our structure definition using Mitsubishi M5M51008 1MB SRAM data. This chip exists in three versions: 0,8 – 0,6 and 0,4 micron. We choose the version A (0,8 μm) for our simulations.

Some technology data were available from reverse engineering performed by NMRC (Construction Analysis DTE1146 part 2 and 3).

The version AVP process can be summarized as follow:

- 0.8 μm polysilicon gate CMOS process.
- No epitaxial layer.
- One level of metallisation.
- METAL 1 is composed of Al with a Ti/TiN barrier layer.
- High resistance SRAM cell.
- There are three levels of polysilicon:
 - Poly 3 is a thin lightly-doped layer which forms the cell resistors.
 - Poly 2 is a normally doped layer which forms the cell ground plane.
 - Poly 1 is a W silicided layer which forms the cell word lines.

Some cross sections of transistor and doping profiles are given hereafter.

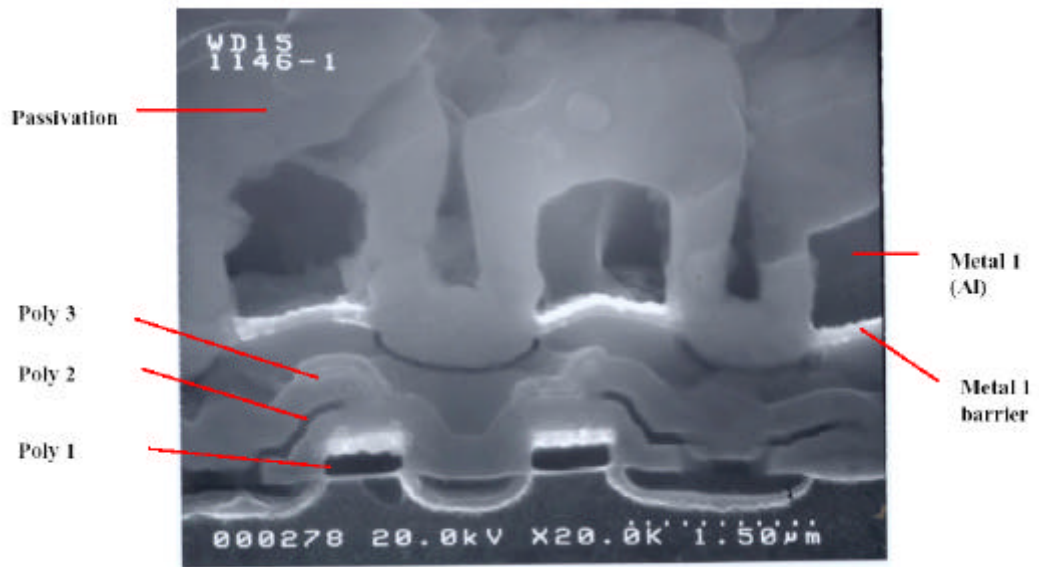


Figure 31: Cross section view of a transistor

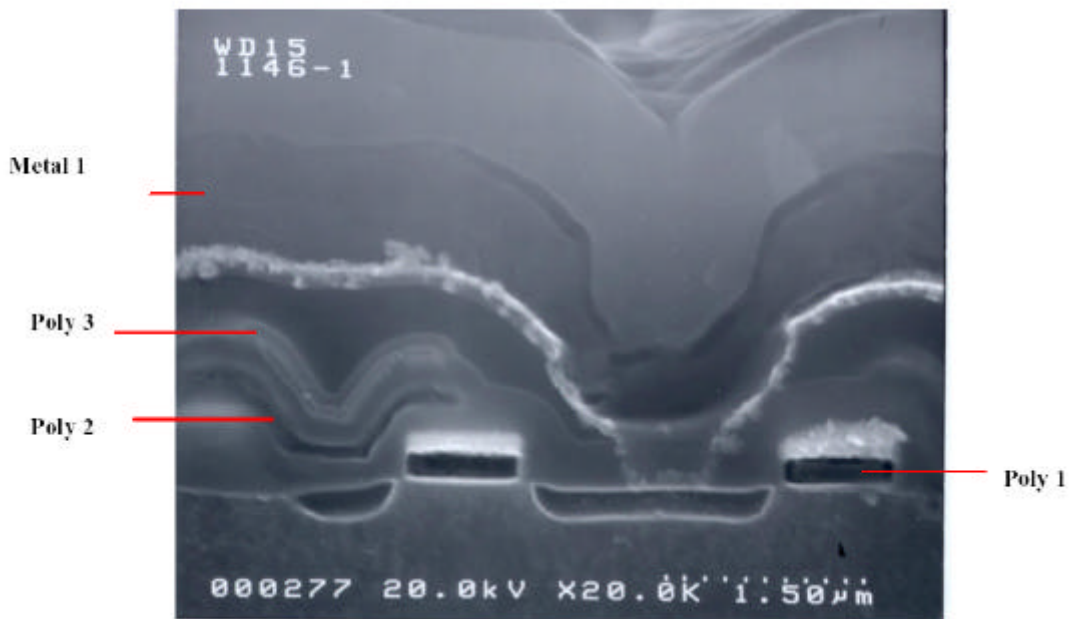


Figure 32: Cross section view of a transistor

Using the following figure, we estimate doping levels of 10^{20} N^+ for the diffusion and a P well of 10^{16} .

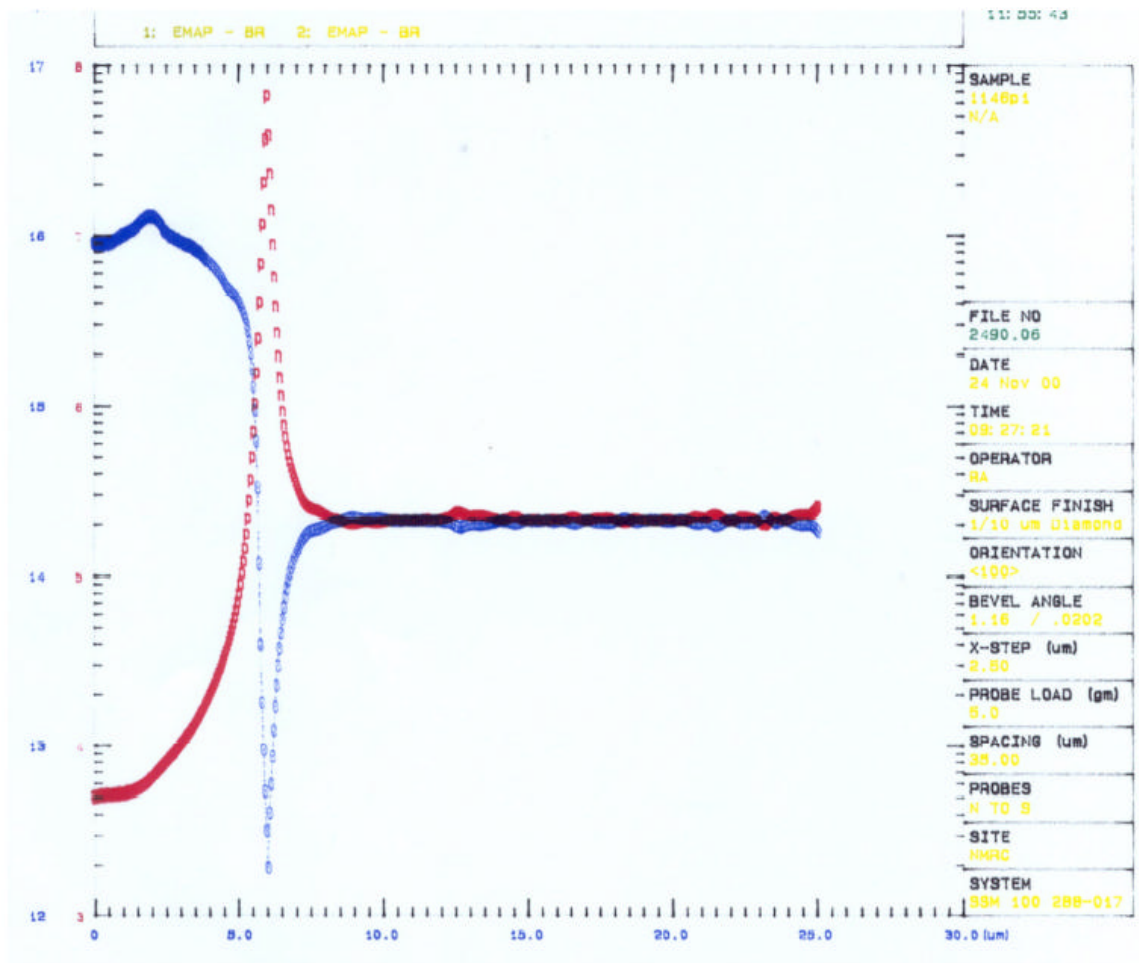


Figure 33: Spreading resistance doping profile well / substrate

Using these data, the following structure was defined. It is worth noting that due to missing full geometry data, it was not possible to simulate a complete memory cell. The following simulations were thus carried out on a single transistor level (dashed blue box in figure 34).

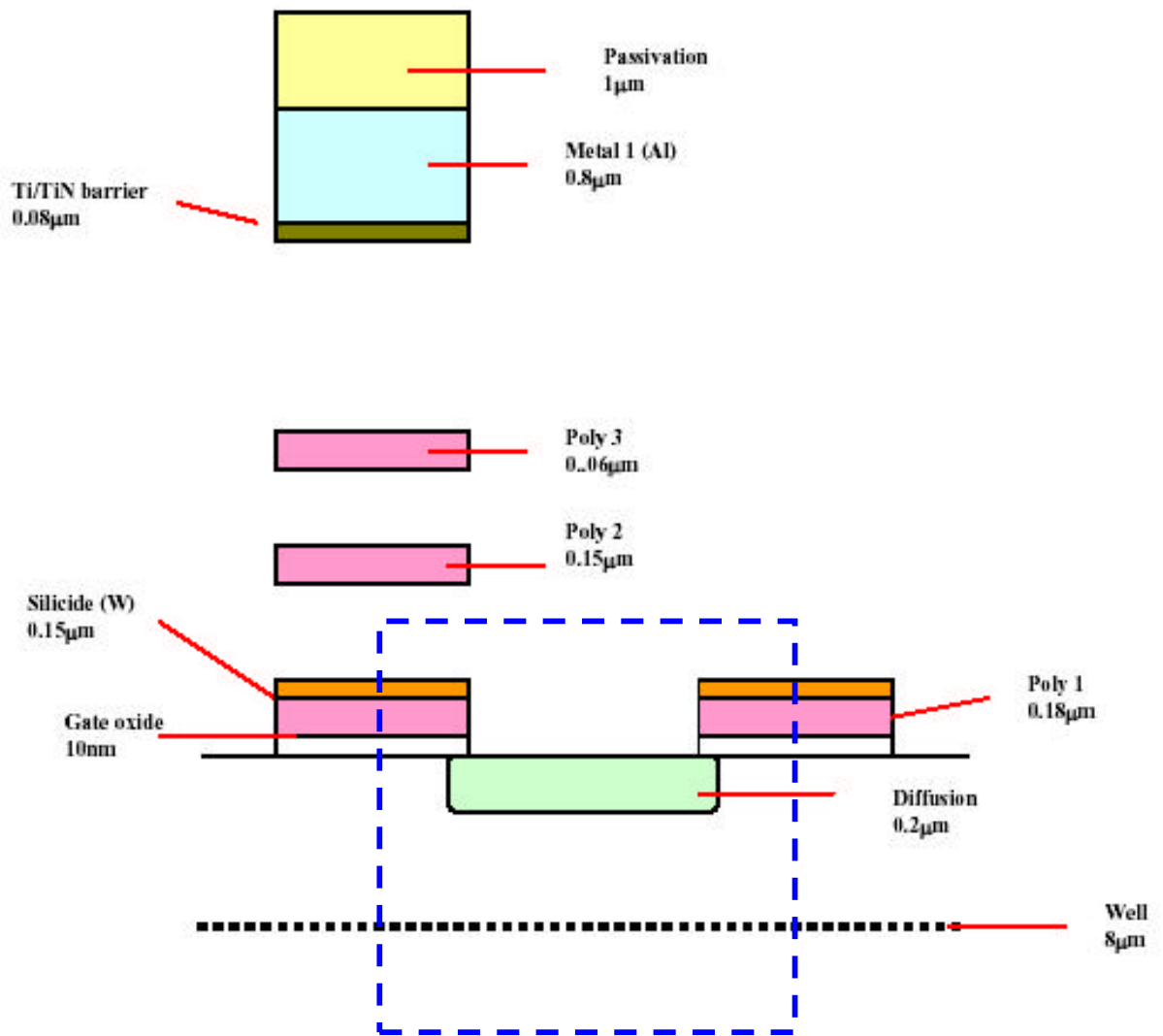


Figure 34: Vertical geometry

4.2 Diode simulations

Figure 35 presents the used meshing as well as the doping profile of the simulated structure. For the first simulations, only a diode structure was used. The third contact was added later (cf. 4.3).

The used beam for the simulations is the same as before (Xe 459 MeV).

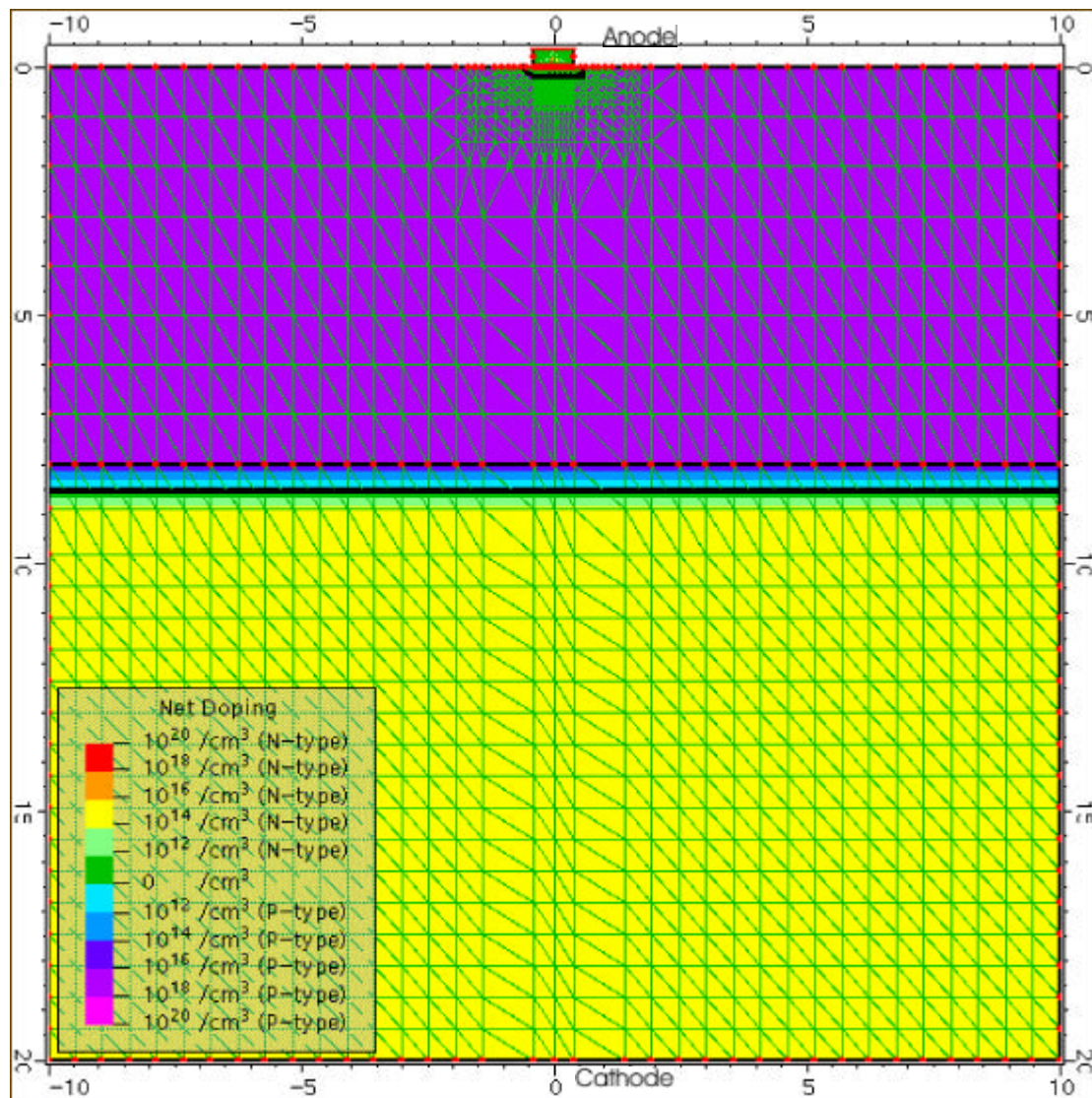


Figure 35: Meshing and doping profile

4.2.1 Ion impact localization influence

The next three figures represent the temporal variation of the photocurrent and anode current for different ion impact localizations. Each ion arrived at normal incidence (perpendicular to the surface).

The 0 μm entry point corresponds to a strike in the middle of the structure, while the $\pm 1 \mu\text{m}$ positions refer to a hit on the side.

In each case, time parameters were kept constant ($T_0 = 4e^{-10}$ s and $T_C = 4e^{-11}$ s.).

Figure 37 presents the cumulative photocurrent, which is the integral of the photocurrent over the time.

Structure is reverse biased at 6V.

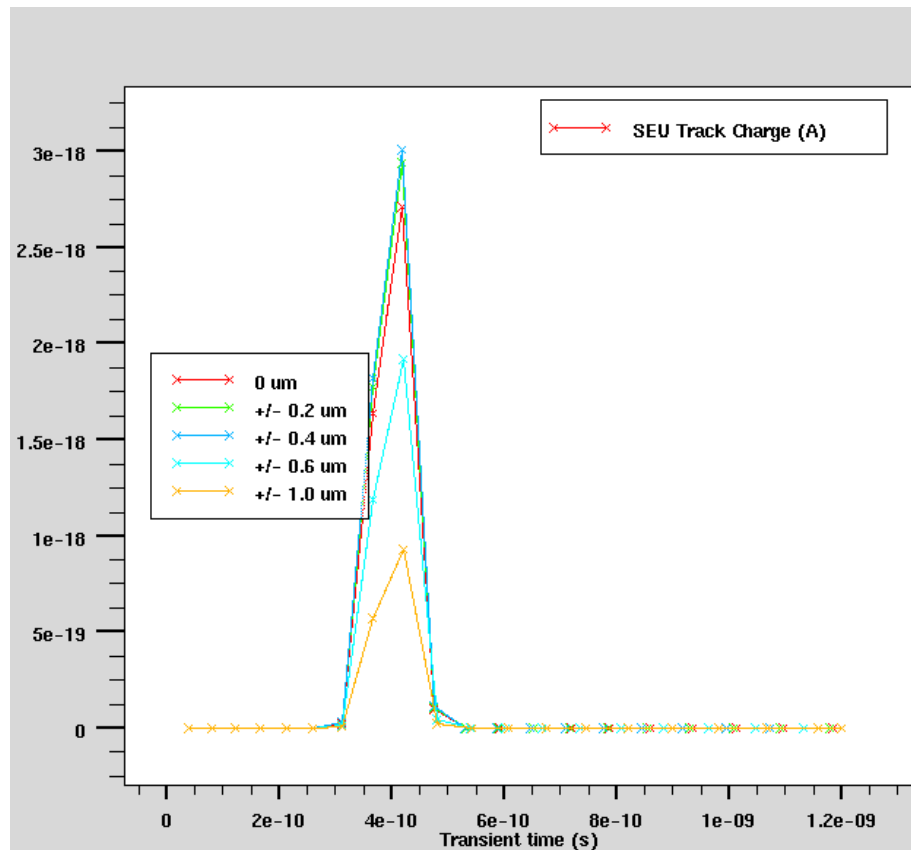


Figure 36: Photocurrent.

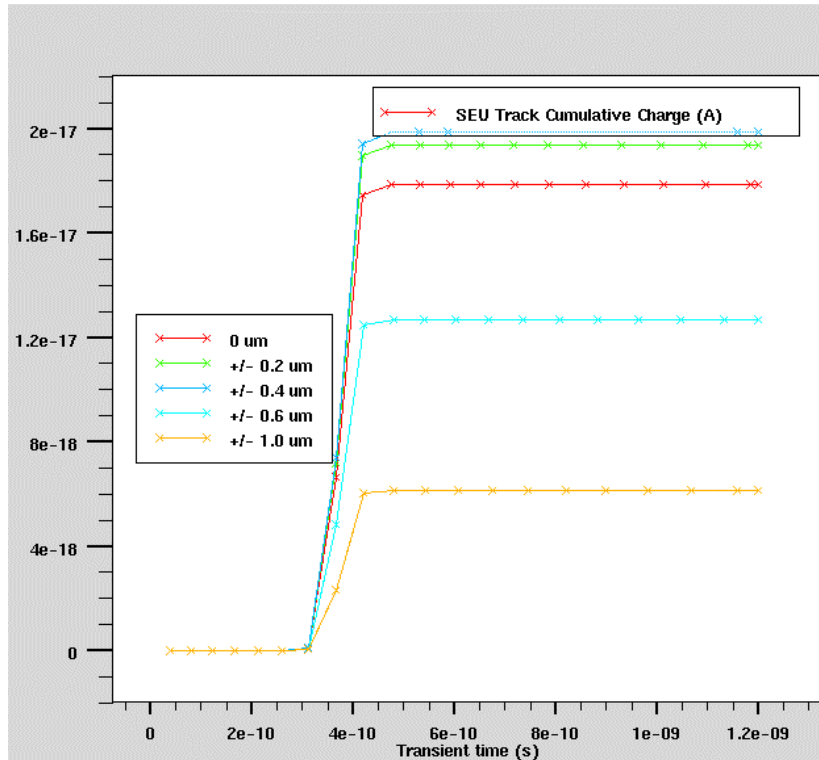


Figure 37: Cumulative photocurrent.

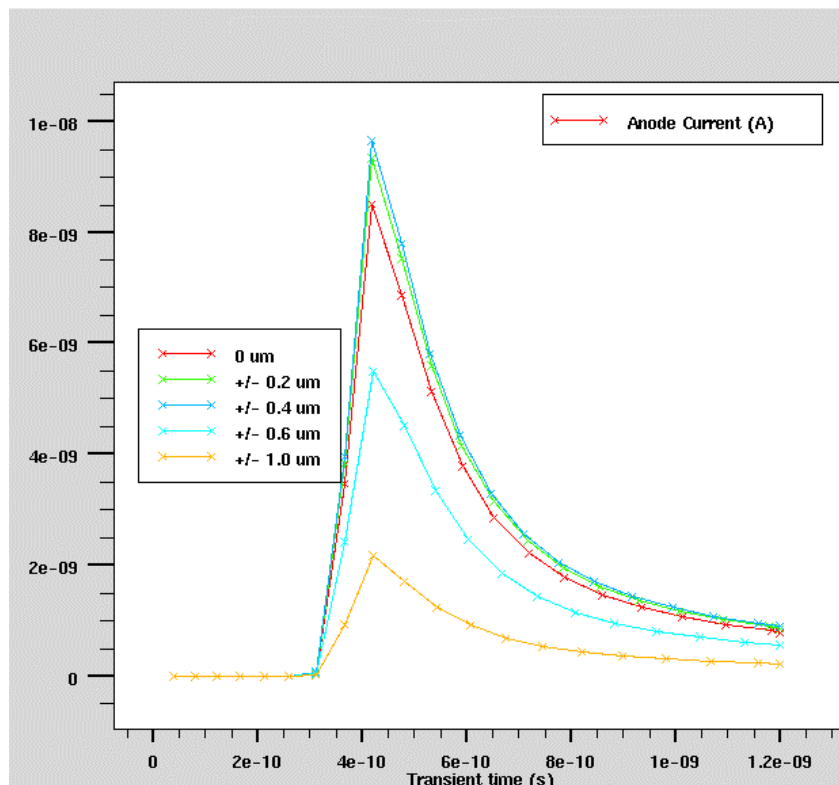


Figure 38: Anode current.

As can be observed, in figure 36 peak value of the photocurrent is large for a centered ion strike, increases while reaching the edge and drop on the side. This tendency is also shown in the cumulative photocurrent (fig. 37).

The anode current presents the same characteristic; maximal for center and edge strikes.

4.2.2 Ion strike time dependence

Next figures present photocurrent and anode current dependencies to time characteristics of the strikes (T_0 and TC). In each figure, sets of two parameters were used. The first one is T_0 (in 10^{-10} s) and the second one TC (in 10^{-11} s).

Structure was simulated reverse biased at -2 V and -10 V

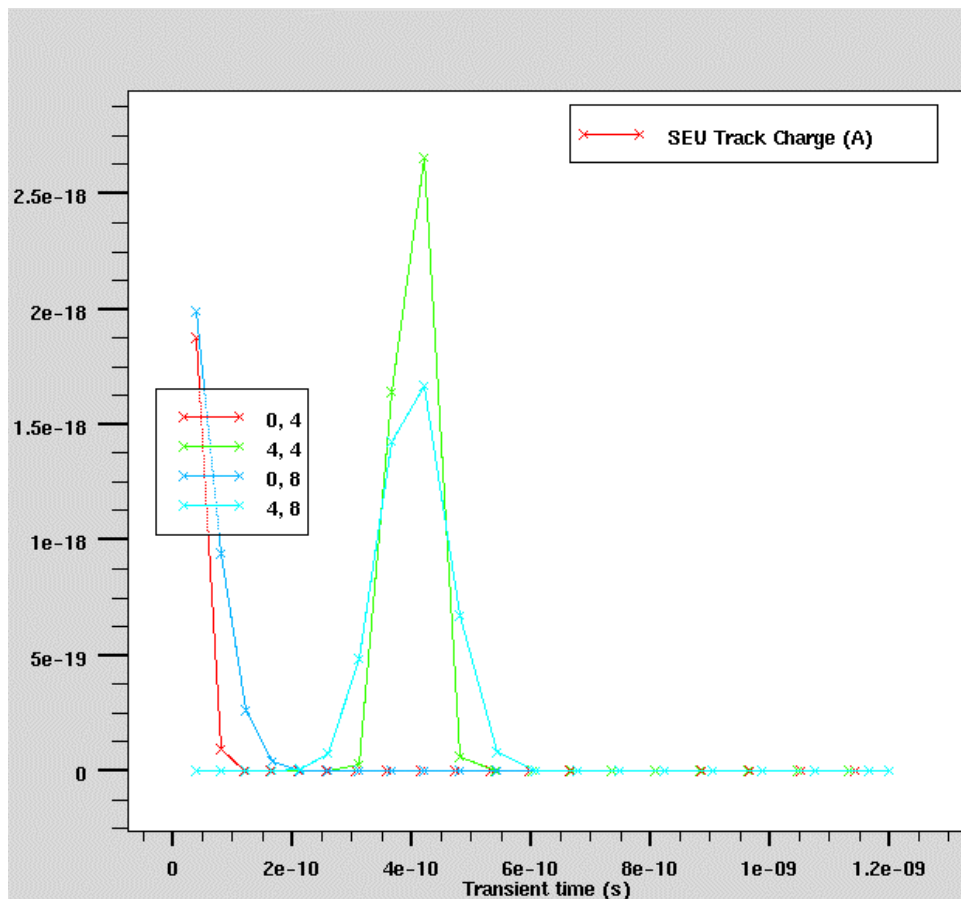


Figure 39: Photocurrent – structure biased at -2 V

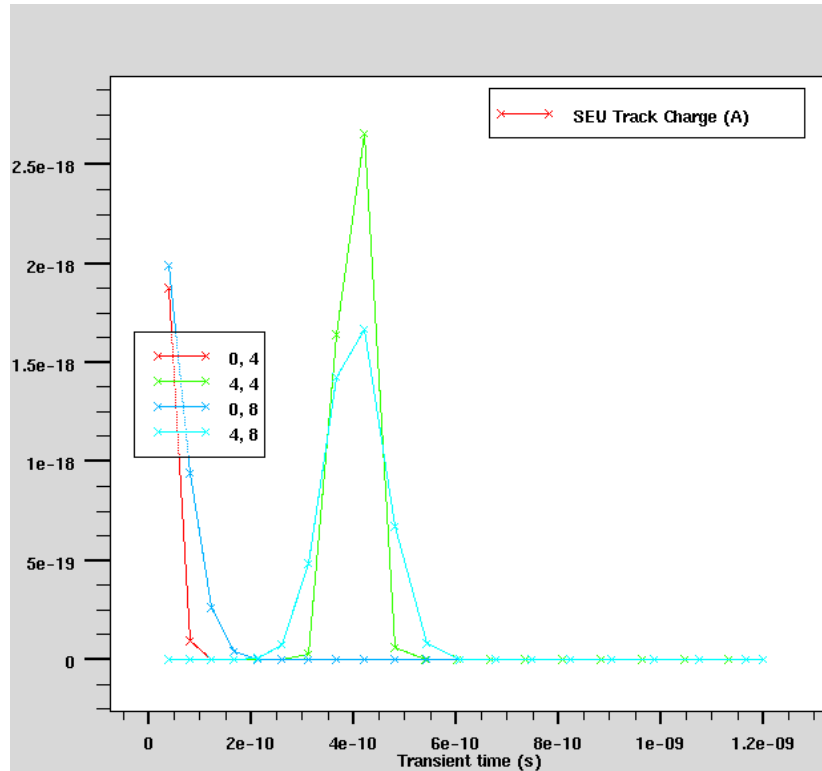


Figure 40: Photocurrent – structure biased at -10 V

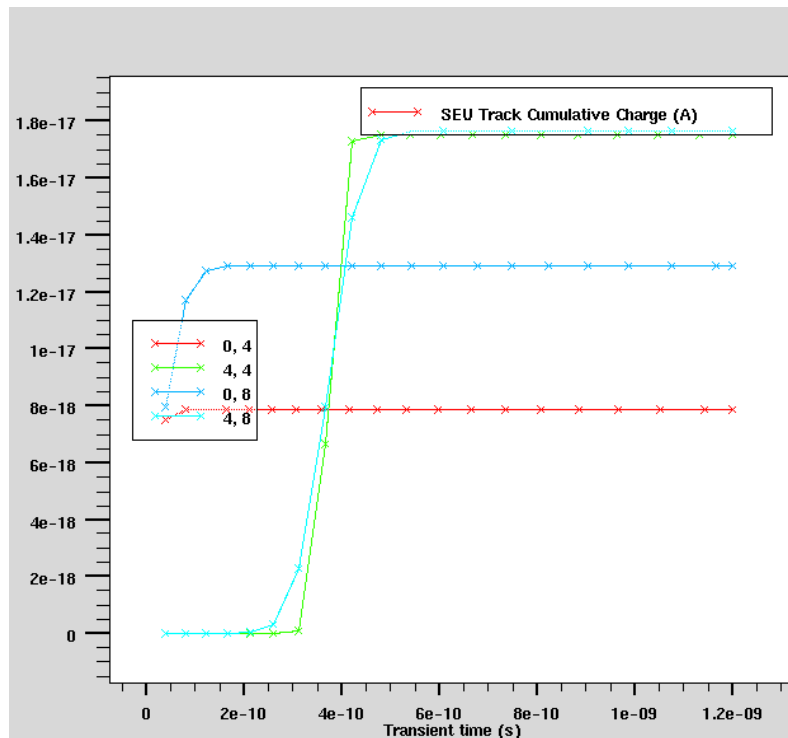


Figure 41: Photocurrent – structure biased at -2 V

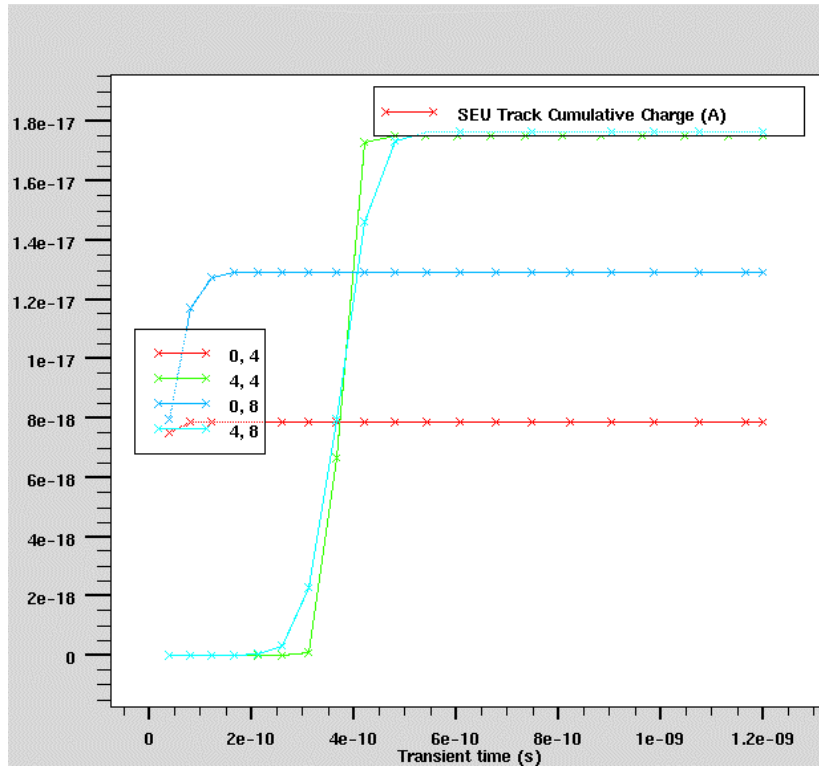


Figure 42: Photocurrent – structure biased at -10 V

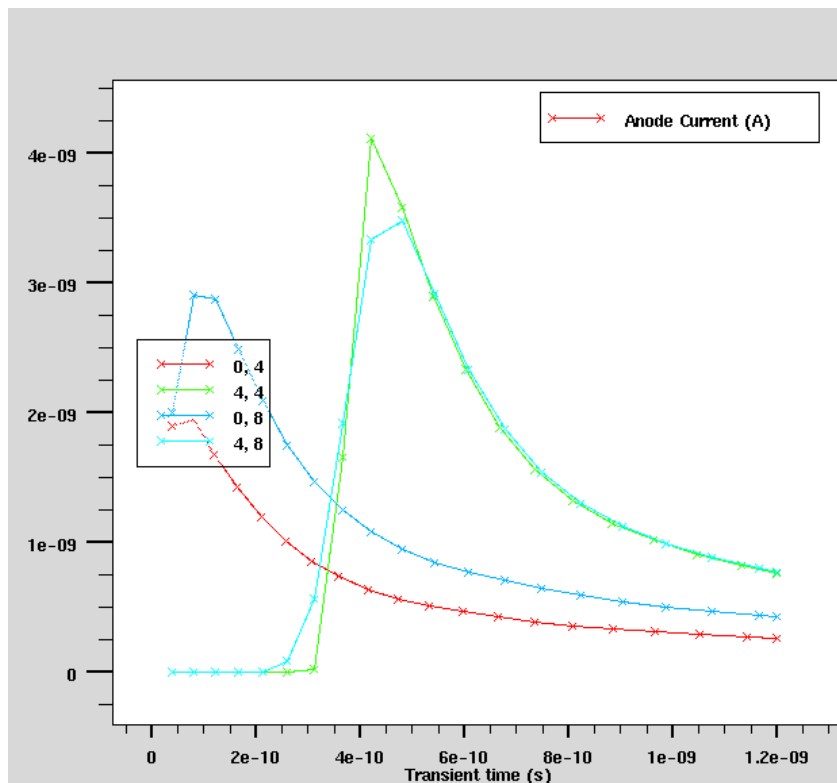


Figure 43: Anode current – structure biased at -2 V

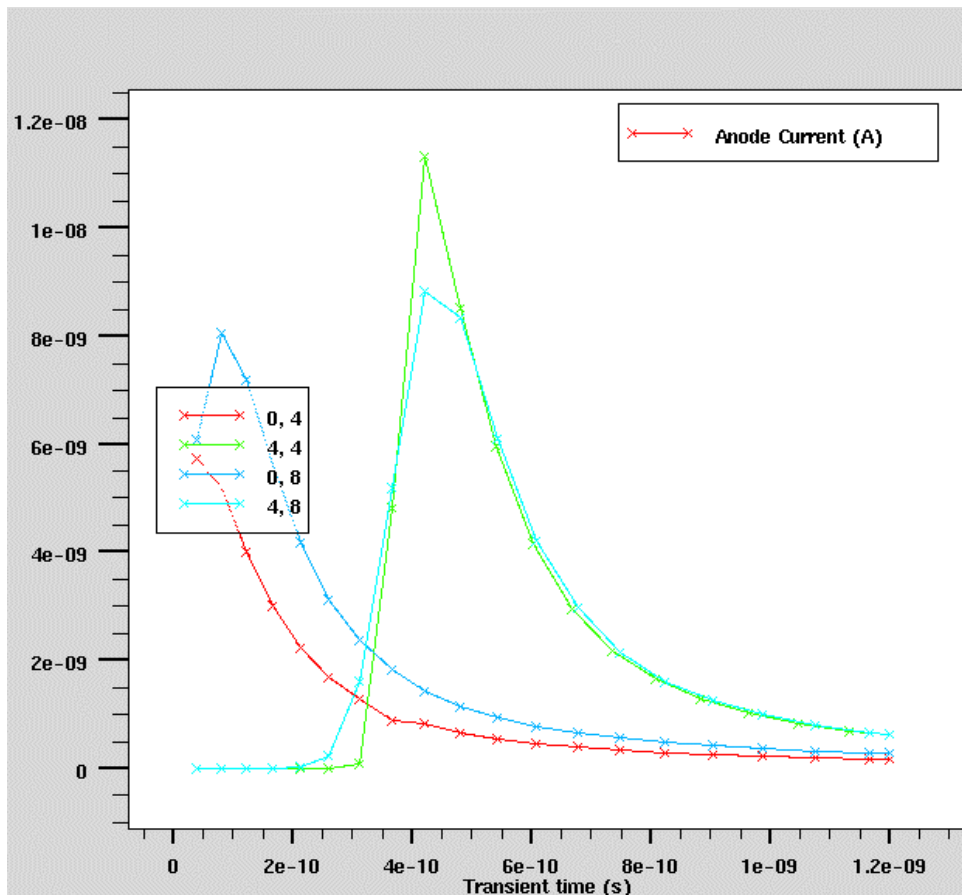


Figure 44: Anode current – structure biased at -10 V

When T_0 is set to 0, a fraction of the photocurrent distribution is missing (fig 39 to 44).

In each photocurrent plot, we see that for the same T_0 , the higher is TC , the higher is the photocurrent.

We can also observe that the bias doesn't influence the photocurrent distribution. In each case, for the same time characteristics, the peak value remains the same. This is not true for the anode current, this one is higher for higher bias.

4.2.3 Reverse biasing influence

The next two figures present anode and cathode current variations for different voltages on the cathode.

In both cases, time characteristics were kept constant: $T_0 = 4e^{-10}$ s and $TC = 4e^{-11}$ s

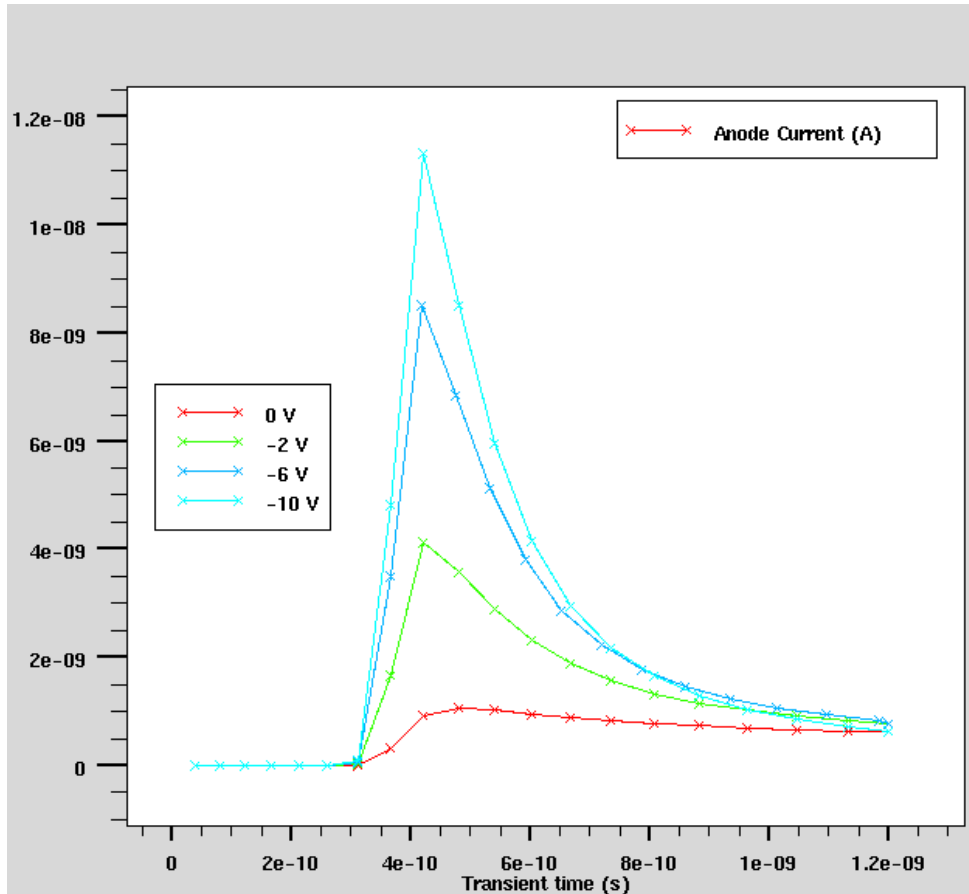


Figure 45: Anode current.

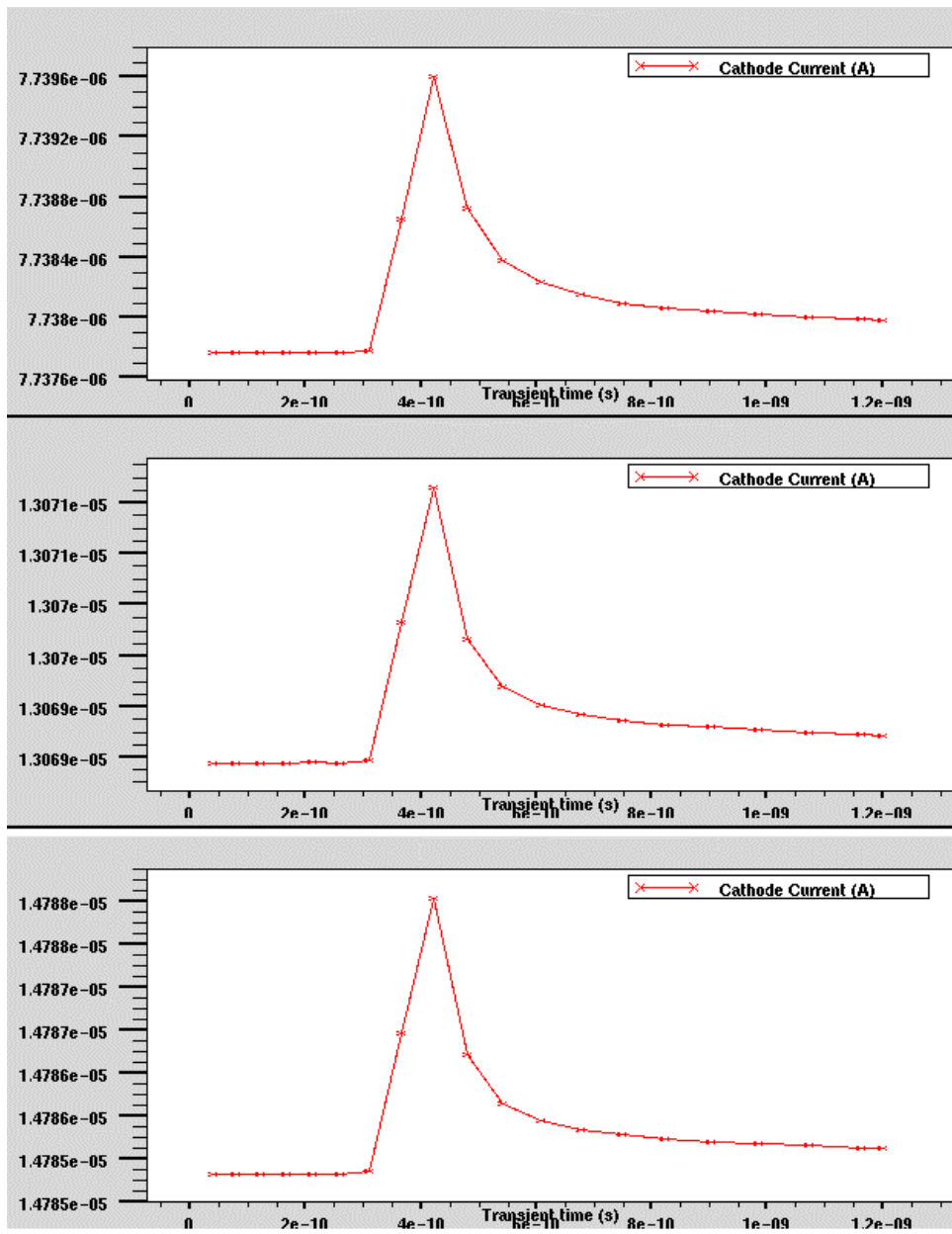


Figure 46: Cathode current for respectively 2V, 6V and 10V on the cathode

The higher reverse bias implies the larger anode current.

While positive biases are used, we observe a modification of the cathode current level linked to the forward polarization.

4.3 Transistor simulations

The following simulations were performed using a half transistor structure. A third contact (Well) was added.

We also observed the effect of the well position on the different currents. The well contact was placed at 5 and 10 (Edge) microns from the center.

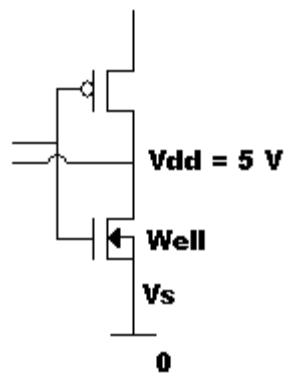


Figure 47: Transistor structure.

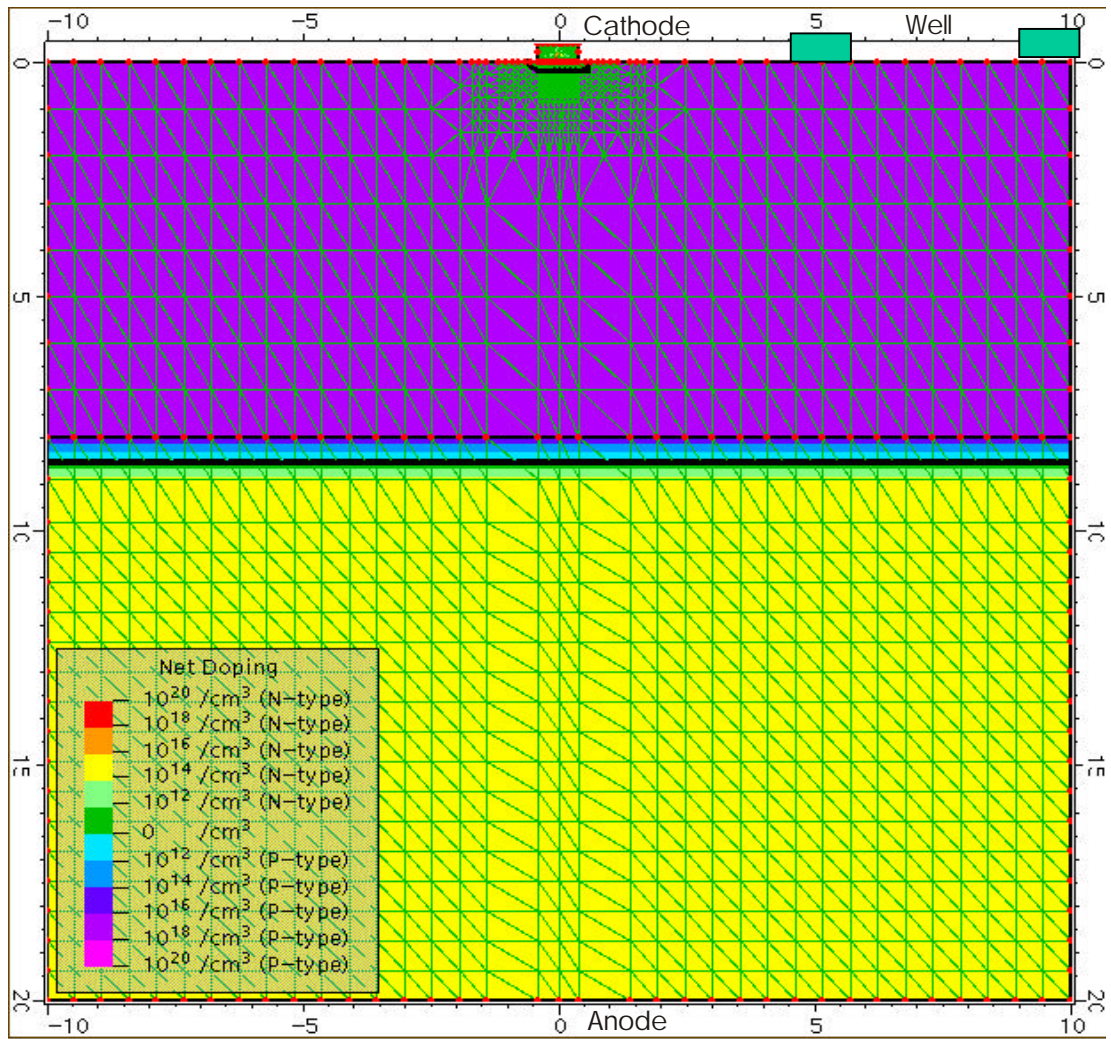


Figure 48: $\frac{1}{2}$ transistor structure.

4.3.1 Well and ion strike localization influence

In the next simulations, two parameters were modified. The ion entry point as well as Well position.

Structure was reverse biased at 6 V, $V_{\text{well}} = V_{\text{substrat}} = 0$ V

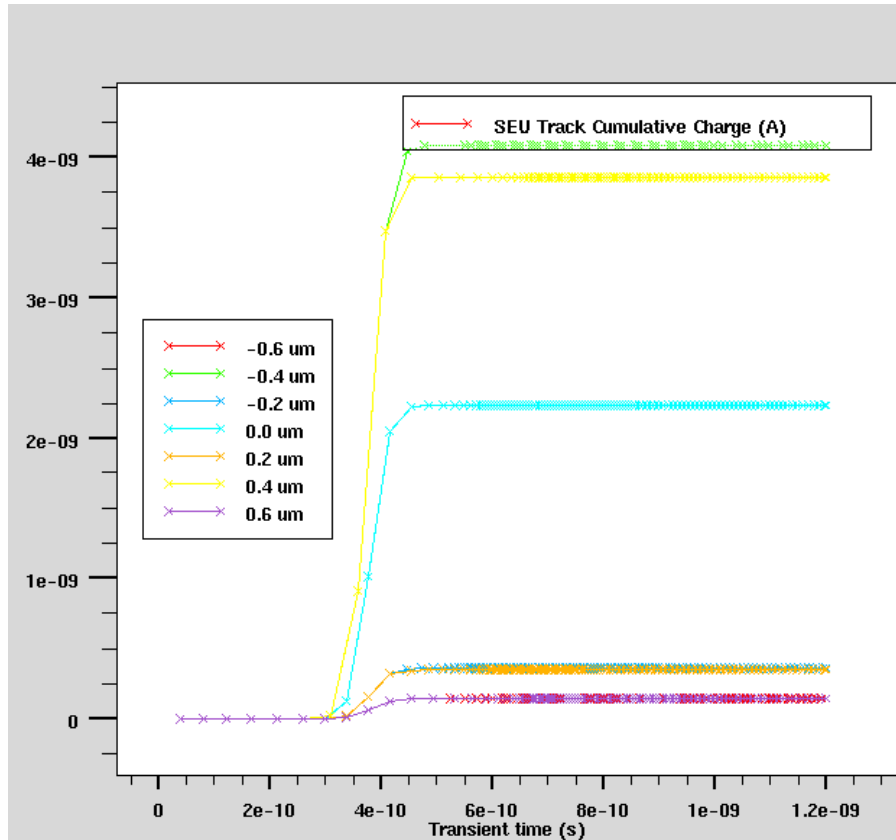


Figure 49: Photocurrent, Well located at 5 μm .

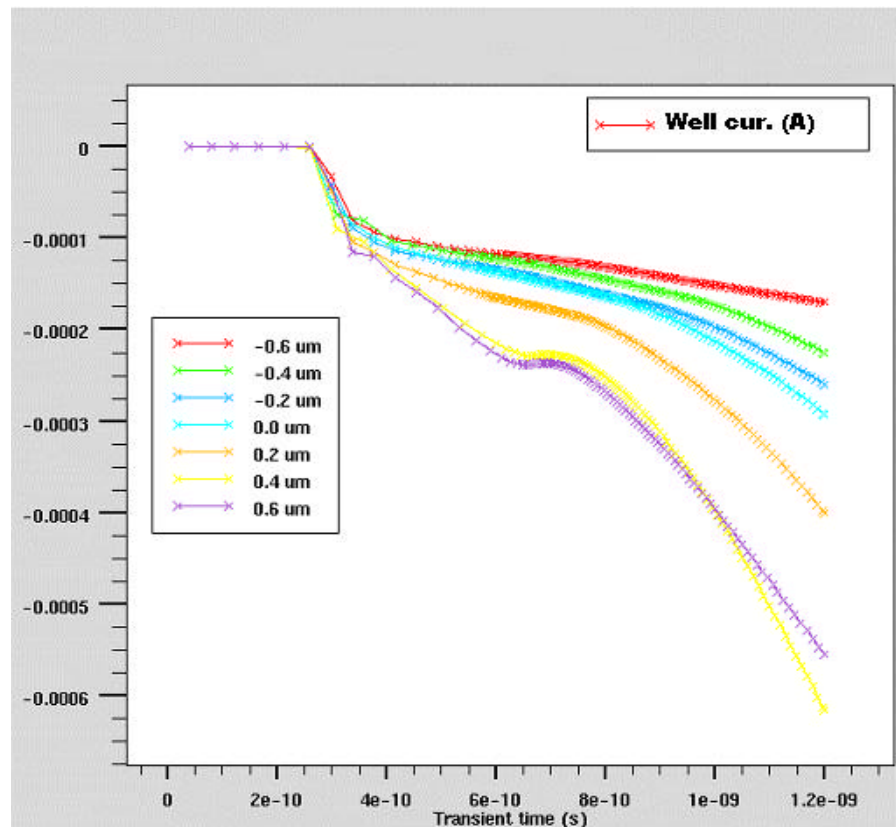


Figure 50 : Well current for Well located at 5 μm .

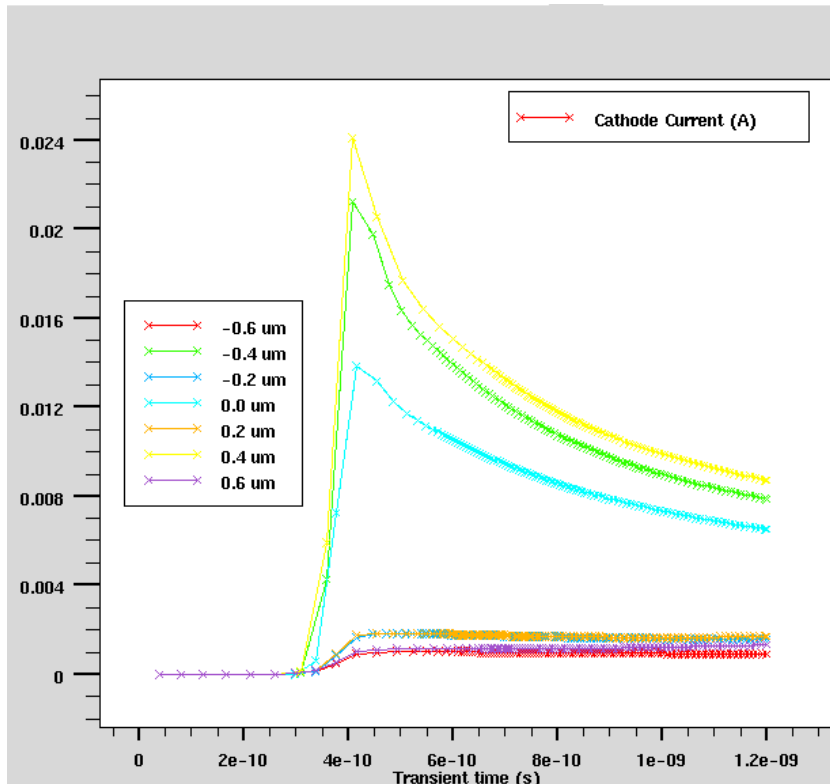


Figure 51: Cathode current for Well located at 5 μm.

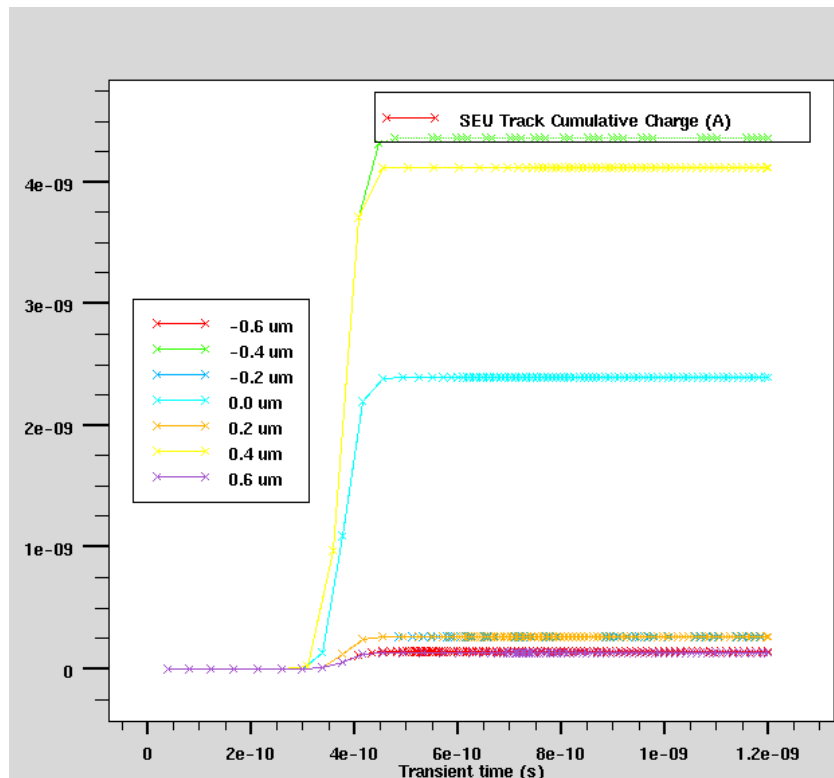


Figure 52: Photocurrent, Well located at 10 μm.

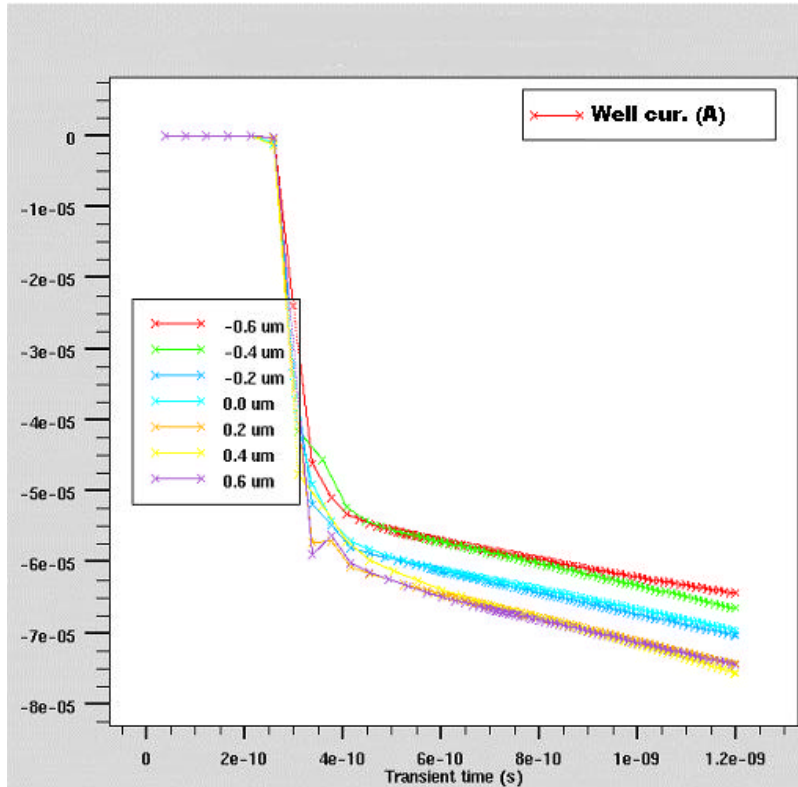


Figure 53 : Well current for Well located at 10 μm.

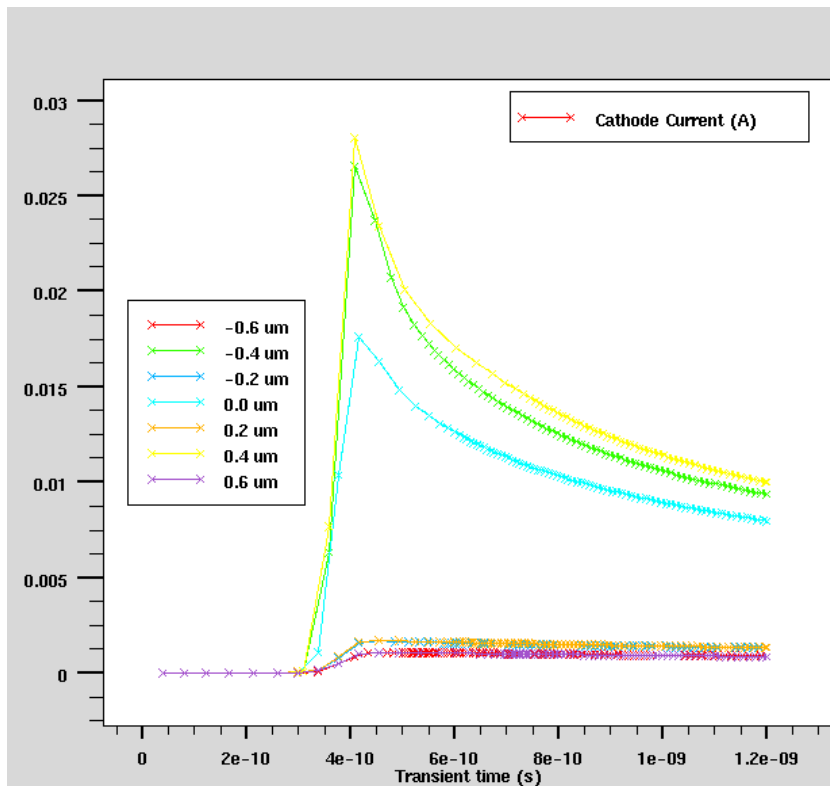


Figure 54: Cathode current for Well located at 10 μm.

Several conclusions can be drawn from these figures:

The cumulative charge is higher for ion strikes located on the same side as the Well and is larger for structure with edge (10 μm) located Well (fig 49 and 52).

The Cathode current peak value is larger for strikes in high inversion region (fig 51 and 54). For the same ion entry point, this current is larger for the 10 μm located Well structure.

Figure 50 and 53 show that the Well current is smaller for edge located Well structure.

4.3.2 Well position and bias influences

Hereafter, different biases were used for the two Well positions (5 and 10 μm).

The figures 55 and 56 represent the cumulative charge and anode current for 0V and reverse biased at -2 V structure.

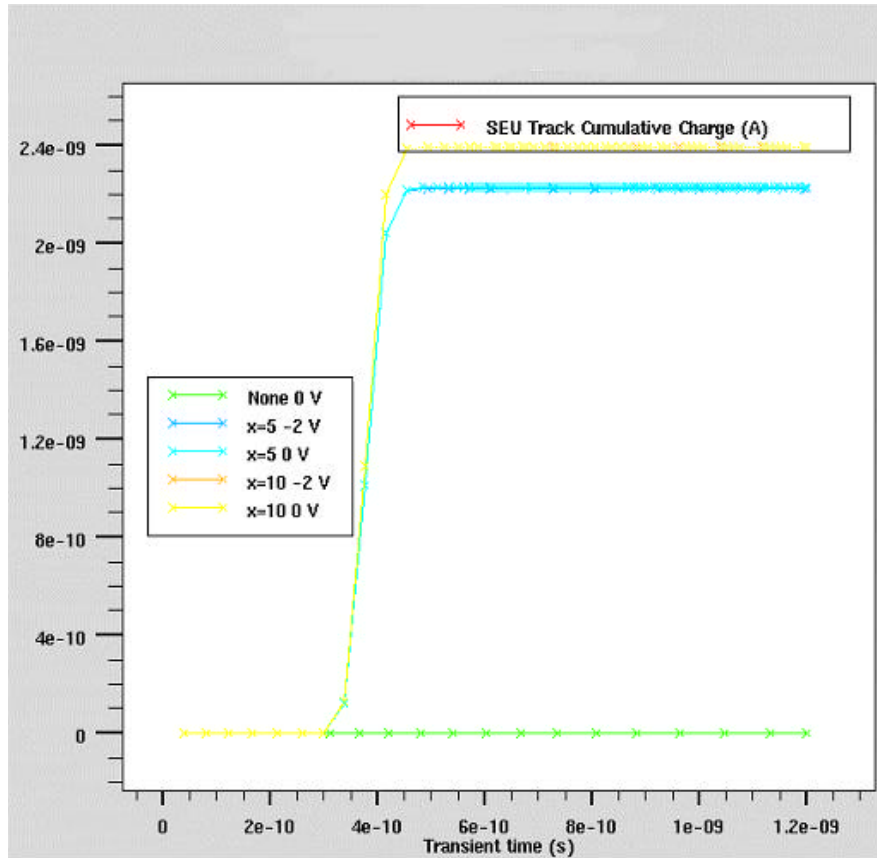


Figure 55: Photocurrent.

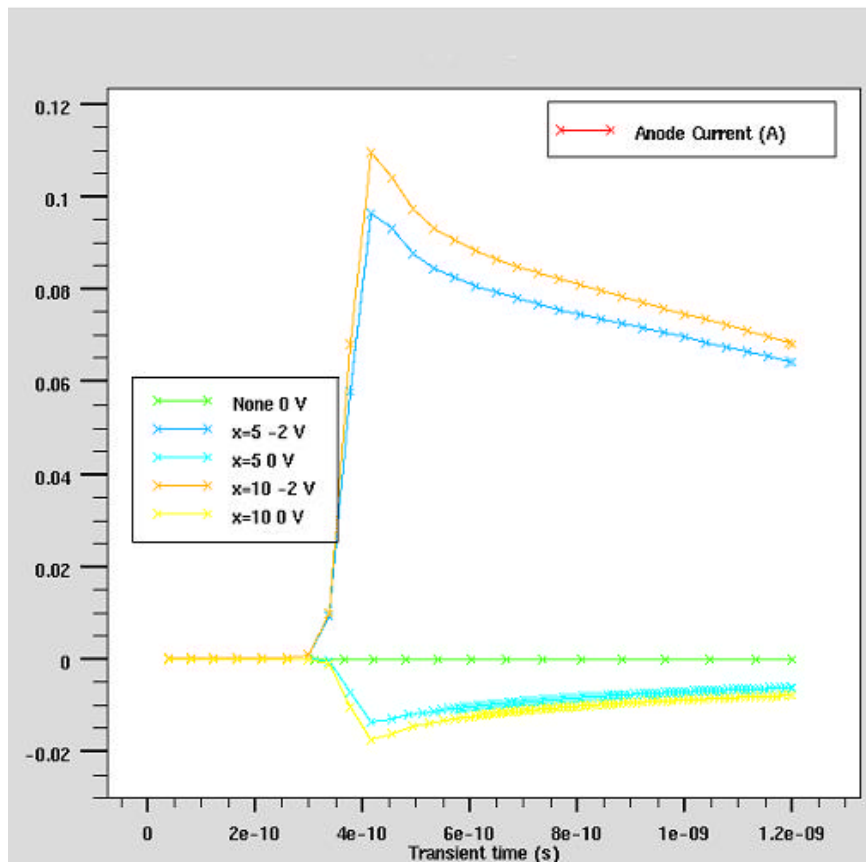


Figure 56: Anode current.

We see that the reverse bias voltage doesn't influence the cumulative charge, while a more negative bias increases the anode current.

We also see that both the cumulative charge and the anode current are higher when the Well is located in the most remote position.

In forward bias conditions, at 2V, the cathode current is larger for edge located Well structures.

4.3.3 Current dependency on ion track angle

Three different structures are analyzed hereafter. For each of them, the ion strike was made for 0° , 30° and 60° . Different entry points have also been selected.

These three structures are without Well contact and with the Well located at $5\ \mu\text{m}$ and at $10\ \mu\text{m}$.

4.3.3.1 No Well contact

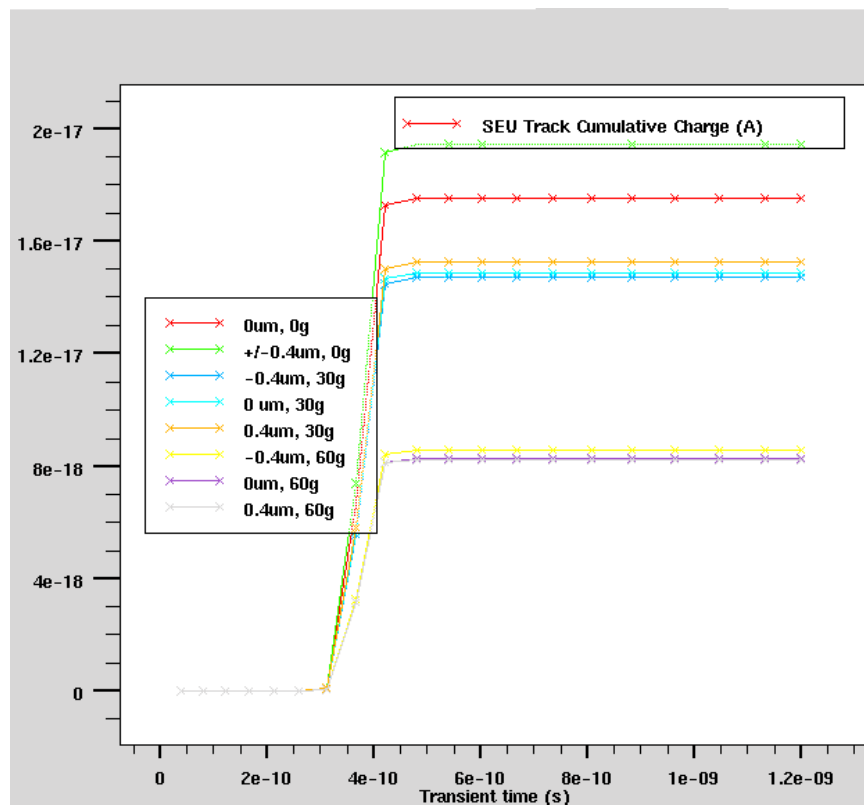


Figure 57: Photocurrent.

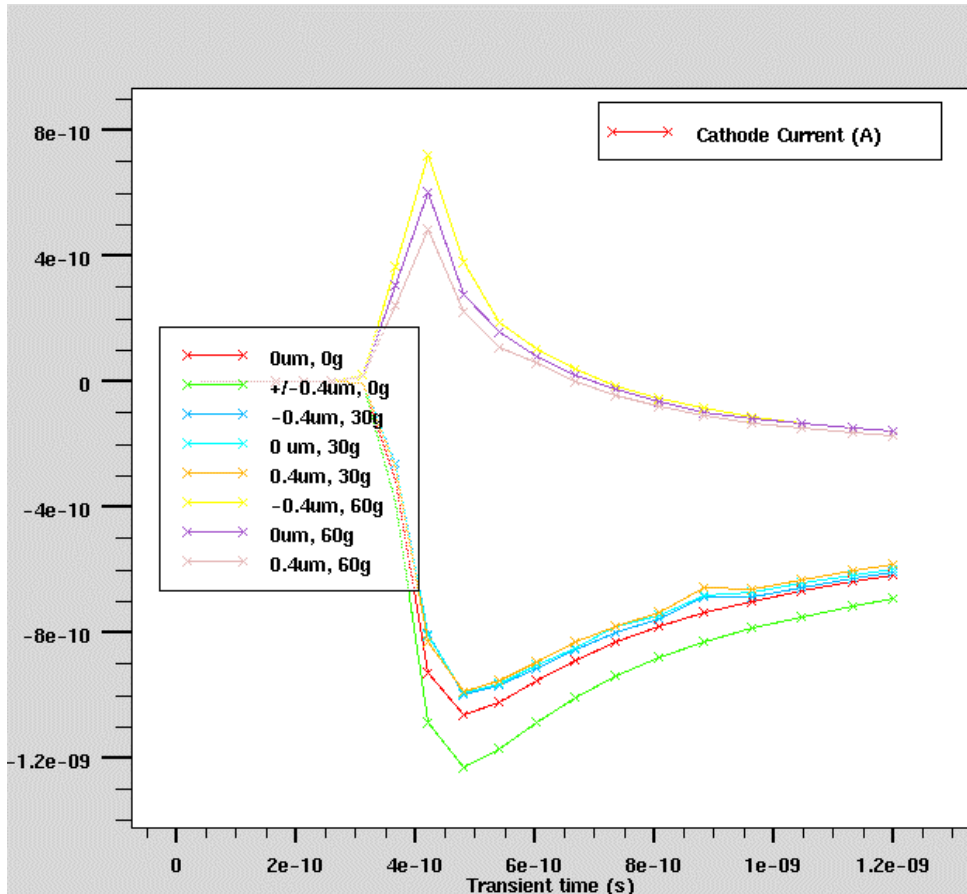


Figure 58: Cathode current

In figures 57 and 58, comparing data for the same entry point indicates lower values for increasing ion track angles. This is well correlated with what has been observed in previous simulations.

We also see that impacts on the edge of the implanted zone induce a larger cumulative charge for a fixed angle.

4.3.3.2 Well contact on the edge

The next simulations present results for an edge located (10 μm) Well structure for different ion entry points and angles.

For each simulation (I_a , I_b , I_c), two graphs are presented; the first one is always a zoom of low dispersion data

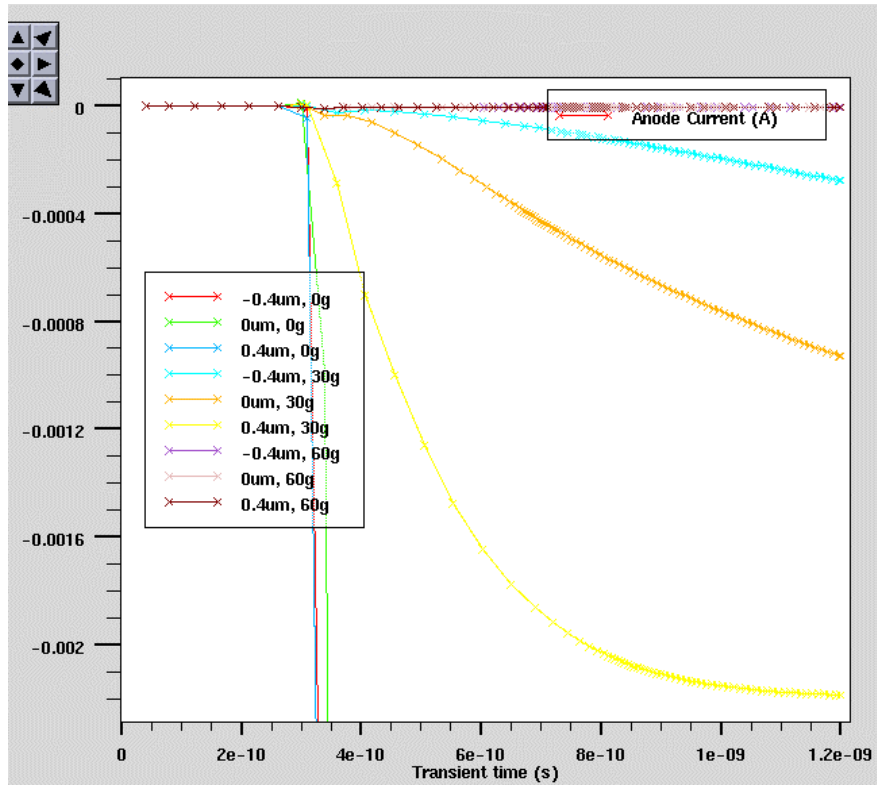


Figure 59: Anode current

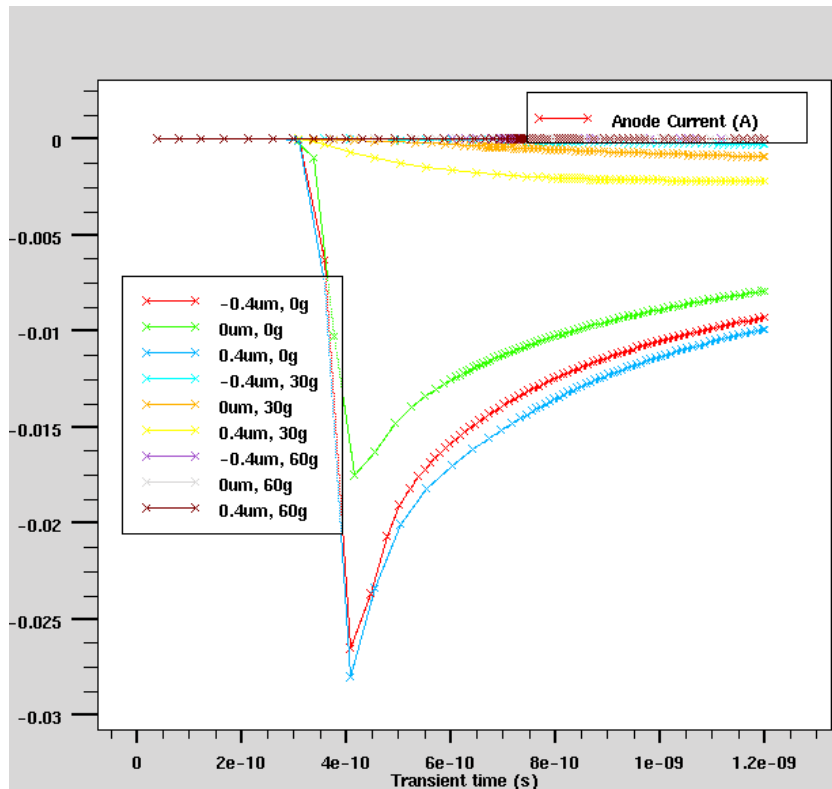


Figure 60: Anode current

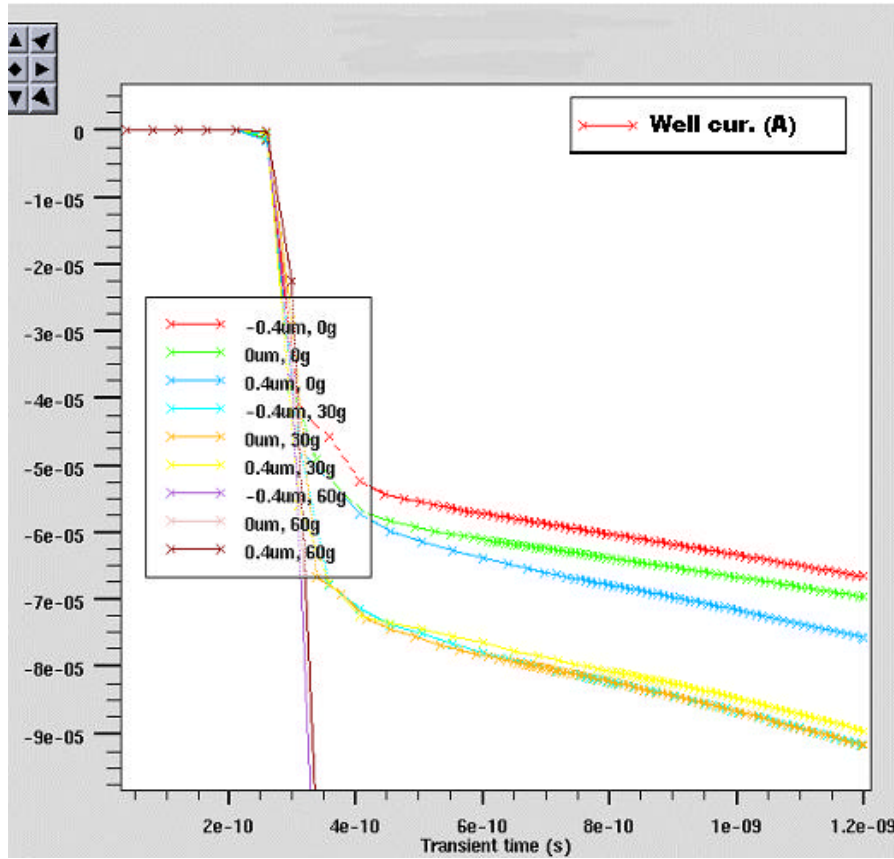


Figure 61: Well current

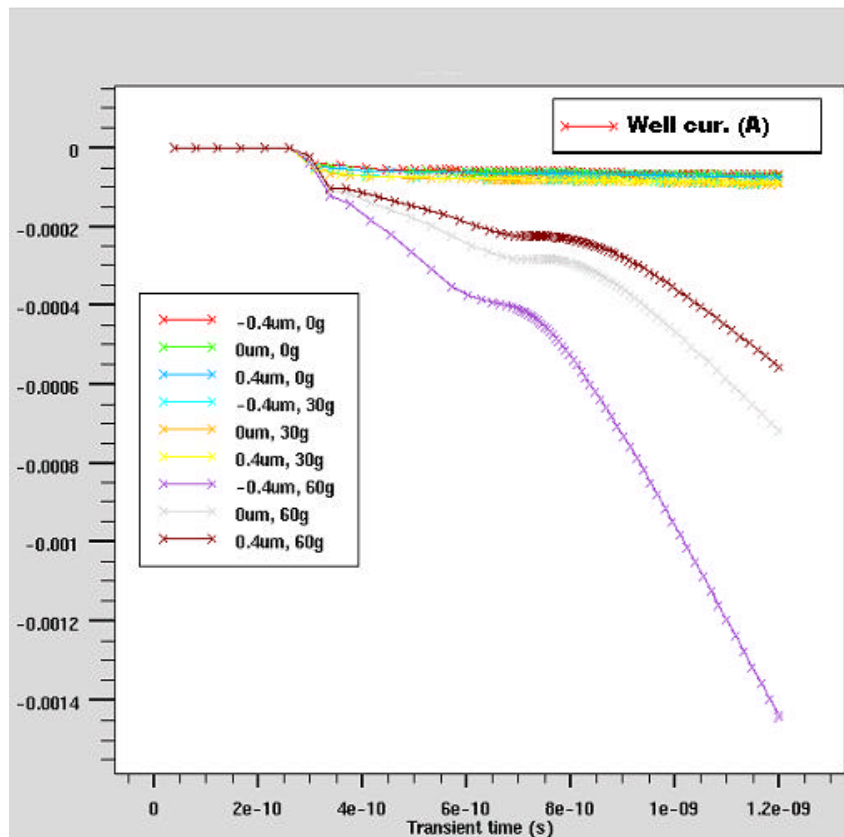


Figure 62: Well current

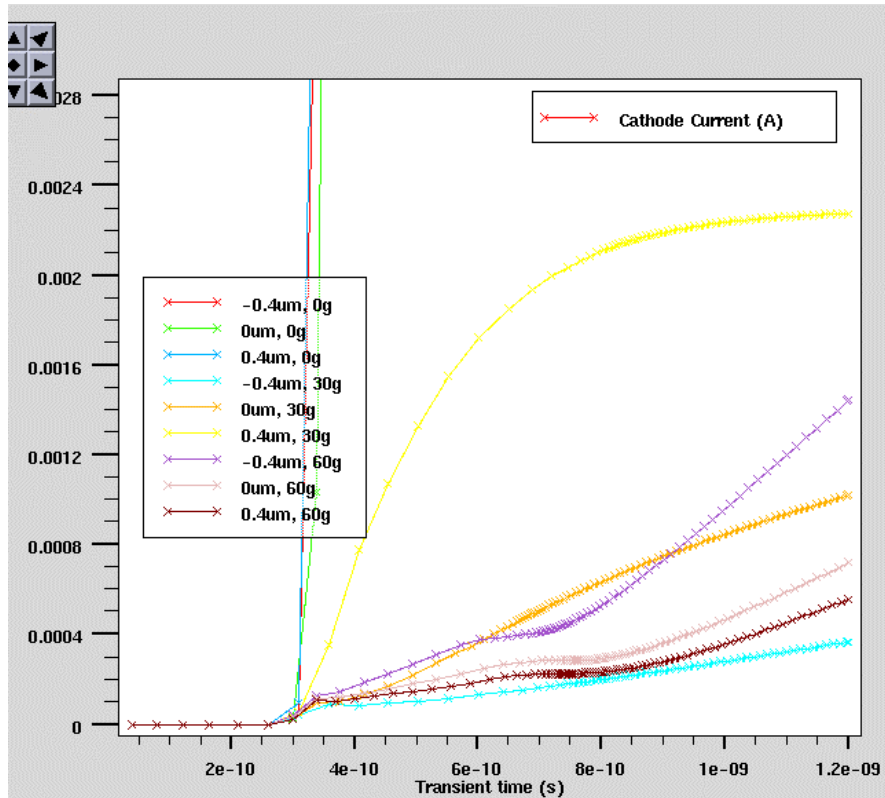


Figure 63: Cathode current

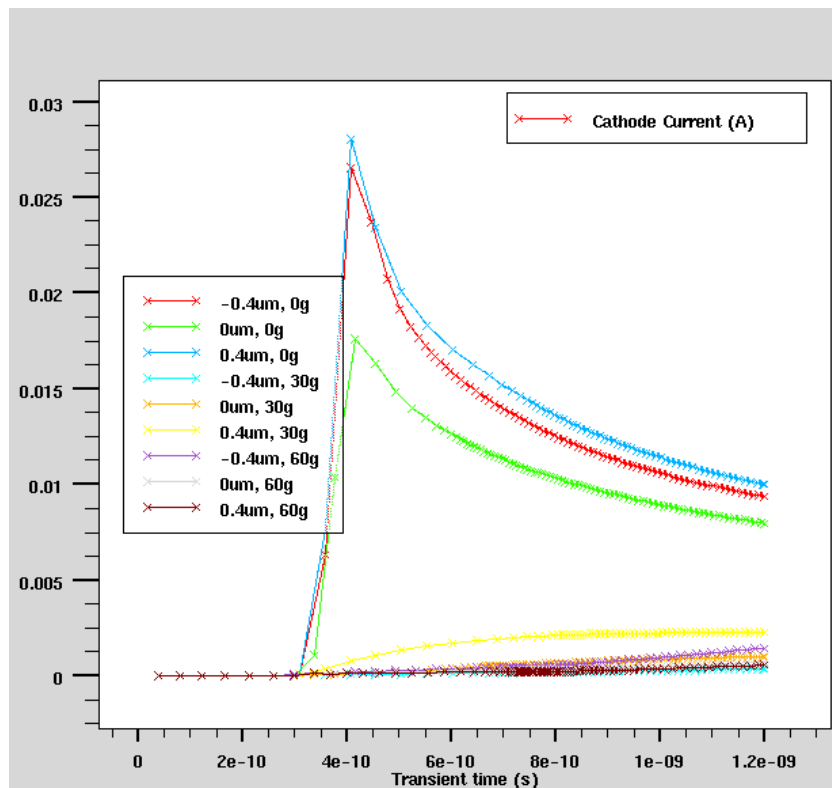


Figure 64: Cathode current

We observe that for a same ion entry point, the Anode currents are larger for larger strike angles. We also see that at the same angle, these currents are larger for entry points located on the edge of the diffusion zone ($0.4 \mu\text{m}$) than in the center. The current is larger for strikes on the Well side ($0.4 \mu\text{m}$), than on the opposite side ($-0.4 \mu\text{m}$) and smaller when ions enter the structure in its middle part.

For the Well current, most negative values correspond to larger incident angles. We can also see that for the same angle, scanning the ion impact position from the Well side to the opposite side lowers the Well current.

The Cathode current on its side is more important for normal incidence strikes.

4.3.3.3 Well contact at $5 \mu\text{m}$

The next simulations present results for the Well located at $5 \mu\text{m}$ structure, for different ion entry points and angles.

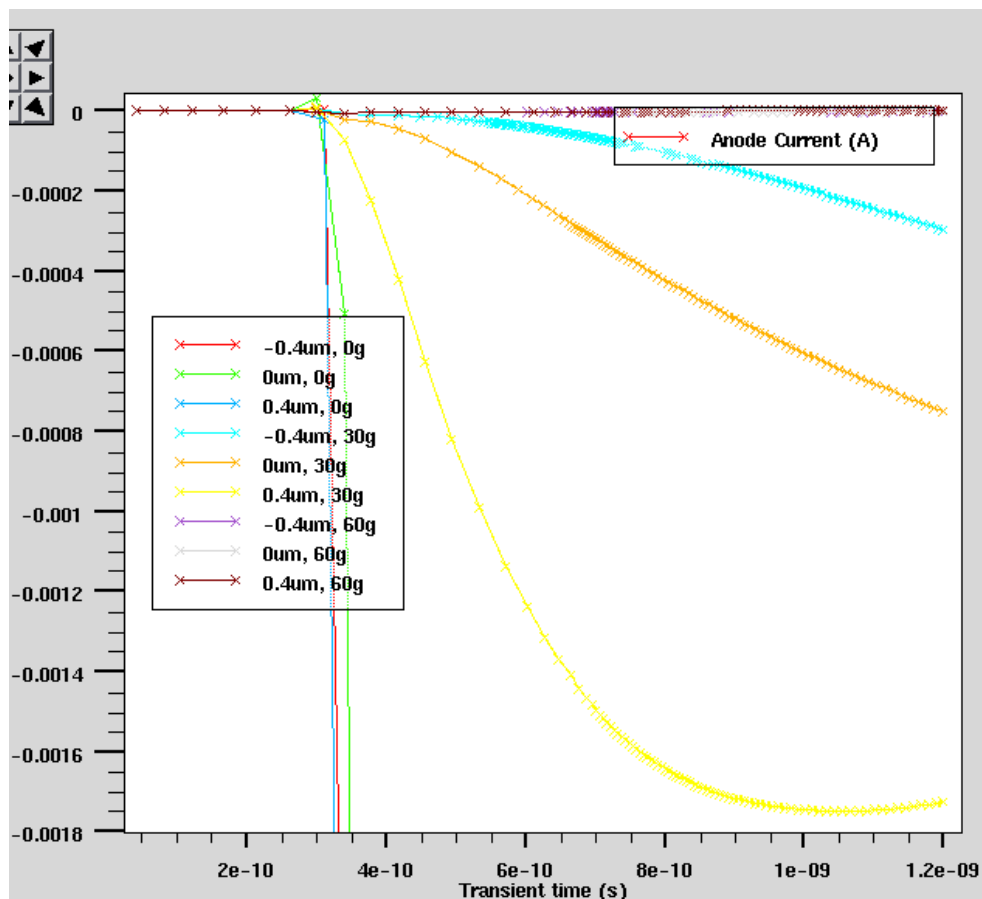


Figure 65: Anode current

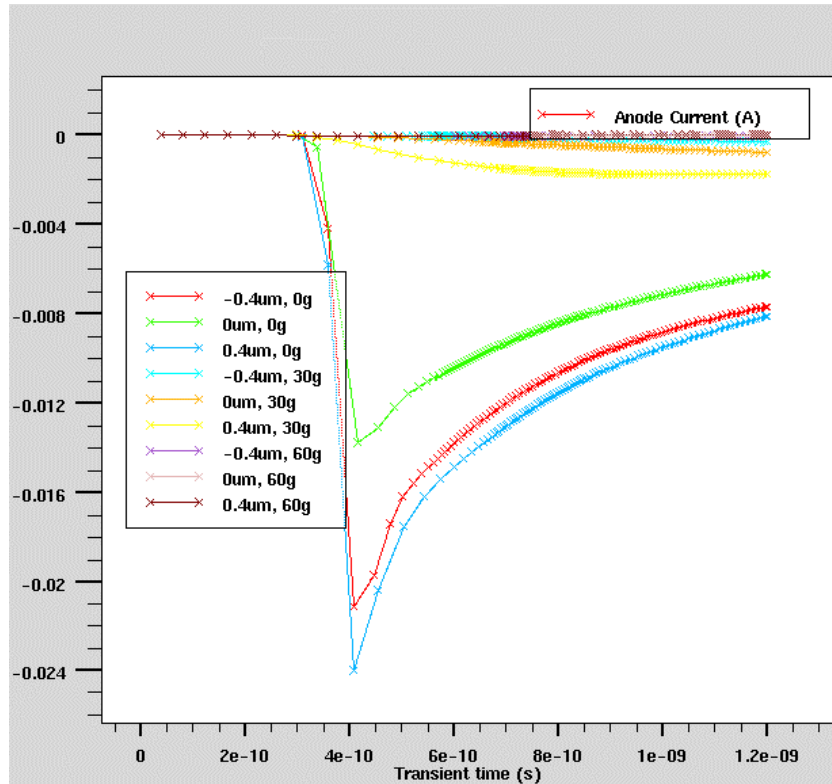


Figure 66: Anode current

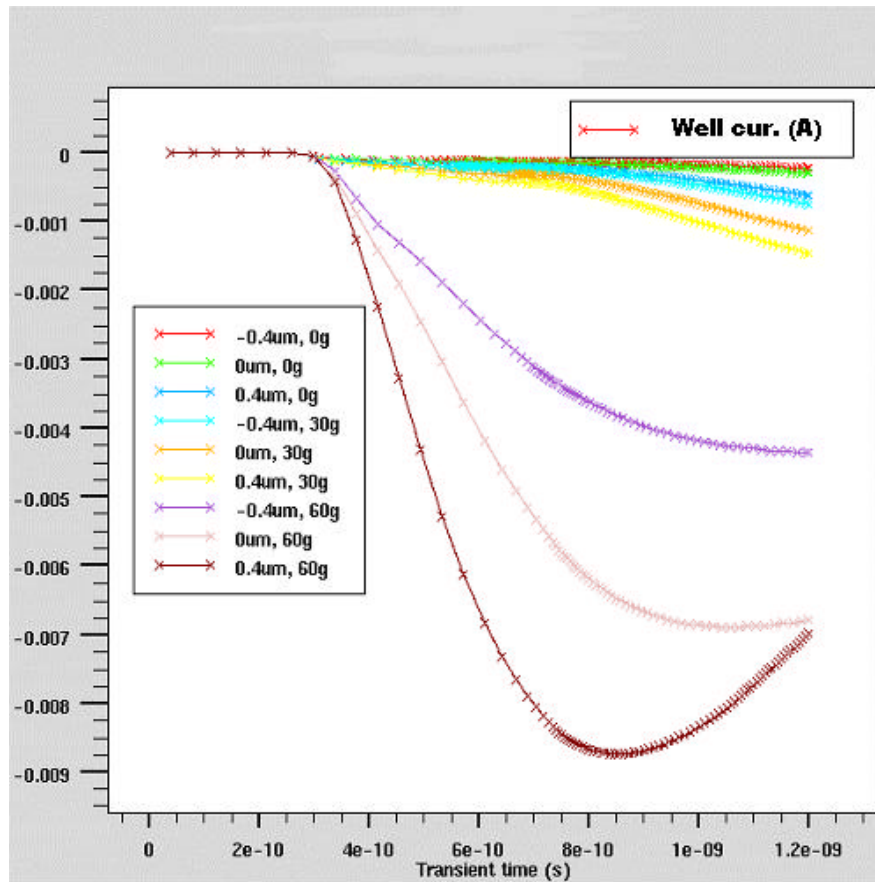


Figure 67: Well current

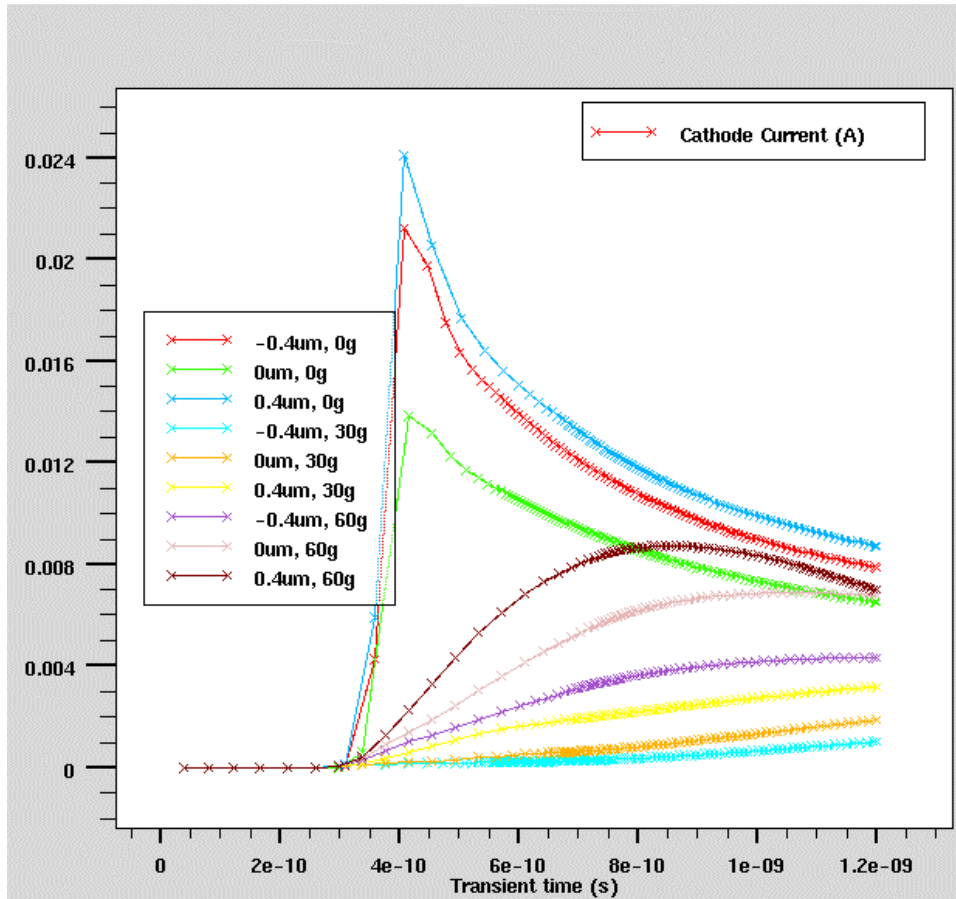


Figure 68: Cathode current

As can be seen on the Anode current curves, the current is larger for increasing strike angles.

The same conclusions can be made for Well current; this one is larger for tilted irradiations. In the same time, this current is more important for ion hits on the edges of the diffusion zone.

The Cathode current on its side is larger for normal incidence ion impacts.

4.3.3.4 Cumulative charge plots

The next simulations present results for the Well located at 5μm and on the edge, for different ion entry points and angles.

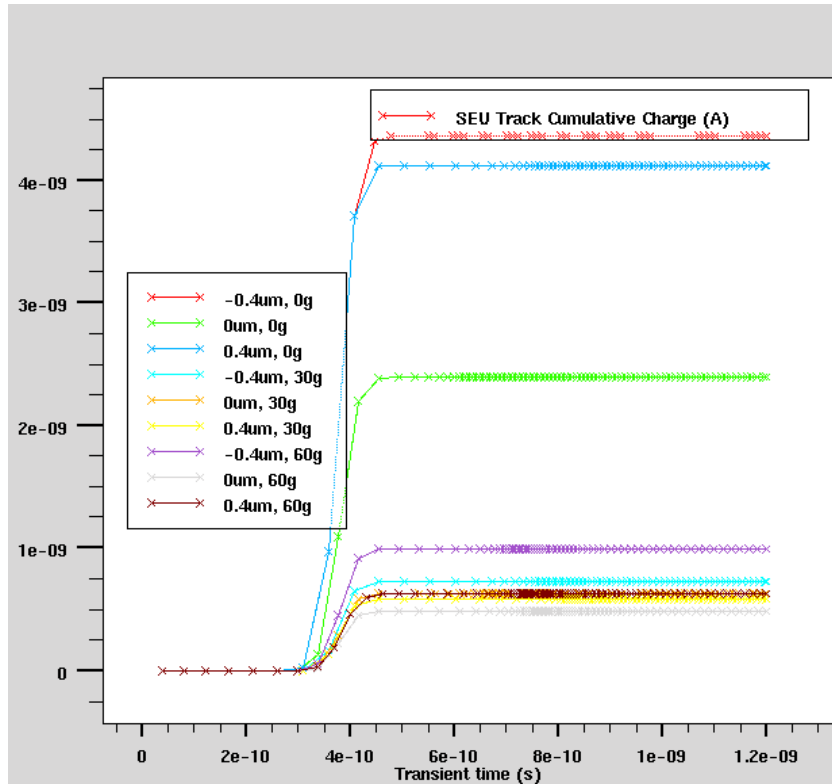


Figure 69: Photocurrent – Well on the edge

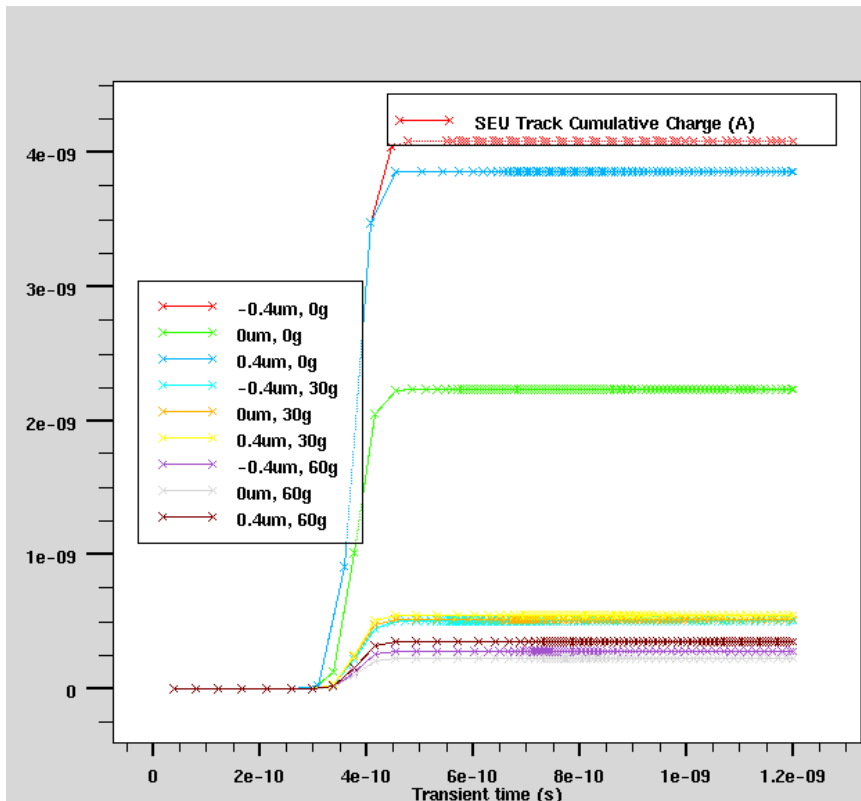


Figure 70: Photocurrent – Well at 5 μm.

These two graphs show that zero degree irradiations induce a larger cumulative charge in both cases.

5. Conclusions

During the different diode simulations, we observed that for normal incidence ion strikes, the photocurrents were higher for centered hits and for impacts at the beginning of the oxide (structure edge).

This “edge phenomenon” is probably linked to the fact that in that high depletion region, created charges move faster to the electrodes.

We also observed that for increasing irradiation angles we obtain a lower current.

Adding a Well contact (as in SRAM transistor structure) produce the same effect, currents were larger for normal incidence.

Time characteristics of the pulses can help to understand this. While tilted, the cathode current modification extends over a longer period of time when compared to normal incidence impact. This may be linked to the fact that for normal incidence strikes, the pairs are generated in the same direction as the current flow, and may have a faster contribution to the cathode current; whereas in tilted conditions, the pairs are created in remote locations from the device main electrical field and take more time to be collected.

These observations are confirmed by the irradiation data. For the same feature size, the collected charge is smaller for tilted conditions than it is for normal incidence strikes.

Experimental data and simulations have demonstrated that the charge collection in PN diodes with CMOS-like shallow junction depth and high substrate doping decrease in amplitude and shows longer time constants when the ion strikes are tilted or on the periphery of the device. This can explain the lower cross section of modern devices for tilted irradiation conditions.

APPENDIX 1. Input file for ATHENA and ATLAS

```
go athena
#

line x loc=0.00 spac=0.2
line x loc=2 spac=0.5
line x loc=9 spac=0.1

#
#line y loc=-0.45 spac=0.0125
line y loc=0.00 spac=0.0125
line y loc=0.2 spac=0.025
line y loc=0.4 spac=0.05
line y loc=1.5 spac=0.25
#
init silicon c.boron=1.0e15 orientation=100
# wet oxidation
#diffus time=2 temp=1000 nitro press=1.00
#diffus time=5 temp=1000 f.n2=1.5 press=1.00
#diffus time=5 temp=1000 dryo2 f.o2=1.5 press=1.00
#diffus time=10 temp=1000 weto2 f.h2=2.8 f.o2=1.5 press=1.00
#diffus time=5 temp=1000 dryo2 f.o2=1.5 press=1.00
#diffus time=20 temp=1000 f.n2=1.5 press=1.00
#diffus time=5 temp=1000 nitro press=1.00

#deposicion de 4500 A de oxido
deposit oxid thick=0.45 divisions=4

# Photoresist deposition
deposit photo thick=1

# Photoresist etching
etch photores right p1.x=3.00

#oxide etching
etch oxide right p1.x=3.00

#residual oxide deposition (300 A)
deposit oxid thick=0.03 divisions=3

#anode implantation ( maxima energia)
implant phosphorus dose=5e15 energy=180 tilt=7 rotation=0
crystal \
    lat.ratio1=1.0 lat.ratio2=1.0
#photores etching
etch photores left p1.x=3.00

# Annealing maximal
diffus time=90 temp=1000 nitro press=1.00
#

#oxide etching
etch oxide right p1.x=3.00
```

```
#metal deposition
#
deposit alumin thick=0.50

electrode name=cathode x=3.50 y=0.00
#
electrode name=anode backside

# plot the structure
struct outfile=prob_00.str
tonyplot prob_00.str

go atlas

models auger consrh conmob fldmob b.electrons=2 b.holes=1
evsatmod=0 \
    hvsatmod=0 boltzman bgn print temperature=300

#
method newton itlimit=25 trap atrap=0.5 maxtrap=4 autonr
nrcriterion=0.1 \
    tol.time=0.005 dt.min=1e-25


solve init
log outfile=prob.log
solve vanode=-0.5
solve vanode=-0.5 vstep=0.05 vfinal=1.5 name=anode
log off
quit
```

APPENDIX 2. Process sheets

n°	Opérations	Gaz	débits	Temps	durée	Epais.	M1	M2	M3
1	Nettoyage standard			1h:00'	0h:45'	4000Å	■	■	■
	H2SO4 / H2O2			10'					
	H2O DI			10'					
	HF 2%			15 sec					
	Oxydation humide 1000 °C (face AV)			4h:00'					
	Entrée	N2	2 l/min	2'	3h:47'				
	Stabilisation	N2	1,5 l/min	10'					
	Oxydation sèche	O2	1,5 l/min	15'					
	Oxydation hum.	O2	1,45 l/min						
		H2	2,8 l/min	155'					
Oxydation sèche	O2	1,5 l/min	20'						
Annealing	N2	1,5 l/min	20'						
Retrait	N2	1,5 l/min	5'						
Chrono :			210'						
3	Ellipsomètre								
4	Nettoyage standard			1h:00'	0h:45'		■	■	■
	H2SO4 / H2O2			10'					
	H2O DI			10'					
	HF 2%			15 sec					
	Dégazage (hydrox2) N2 800°C			0h:15'					
Entrée	N2	1,5 l/min	2'	0h:32'		■	■	■	
Dégazage	N2	1,5 l/min	15'						
Retrait	N2	1,5 l/min	5'						
Chrono :			15'						
6	Photolitho Ndiff				3h:00'		■	■	■
	Enduction 3500 rpm								
	Exposition								
	Développement			90 sec					
	Barrel 150W / O2 : 42%			60 sec					

7	Décapage OxydeBuffer HF 630 A/min Buffer HF Rinçage H2O DI	6' 30" 10'		
8	Implantation Phosphore	180KeV 5e15		
9	Implantation Phosphore	100KeV 5e15		
10	Implantation Phosphore	20KeV 5e15		
11	Décapage résine H2SO4 Décapage résine H2SO4 Nétoyage sans HF			
12	Barrel 10mn 500W			
13	Nettoyage standard			
14	Anneling T=1000°C sous N2	1h:30'		
15	Anneling T=1000°C sous N2	30'		
16	Anneling T=1000°C sous N2	1h:00'		
17	Nettoyage standard			
18	Dépôt nitrure PECVD		1000 A	
19	Photolitho Poly1 Enduction 3500 rpm Exposition Développement Barrel 150W / O2 : 42%	90 sec 60 sec	3h:00'	
20	Gravure nitrure			
21	Décapage résine H2SO4 Décapage résine H2SO4 Nétoyage sans HF			

22	Nettoyage standard			1h:00'					
	H2SO4 / H2O2			10'					
	H2O DI			10'					
	HF 2%			15 sec	0h:45'				
23	Dégazage (hydrox2) N2 800°C			0h:15'					
	Entrée	N2	1,5 l/min	2'					
	Dégazage	N2	1,5 l/min	15'					
	Retrait	N2	1,5 l/min	5'	0h:32'				
	Chrono :			15'					
24	Photolitho Contact								
	Enduction 3500 rpm								
	Exposition								
	Développement			90 sec					
	Barrel 150W / O2 : 42%			60 sec	3h:00'				
25	Gravure plasma oxyde								
26	Décapage résine H2S04								
27	Métallisation Al/Si					10000Å			
28	Photolitho Metal		masque MEMS1						T2
	Enduction 5600 rpm								
	Promoteur pyrox								
	Exposition								
	Développement			90 sec					
	Barrel 150W / O2 : 42%			60 sec	3h:00'				
29	Gravure aluminium plasma					10000Å			T2
30	Décapage résine acide nitrique			0h:10'					
31	Tests contacts								
32	Recuit Al 420 °C N2+H2 (face AV)			0h:20'					
33	Dépôt couche de passivation oxyde APCVD								T3
34	Photolitho Pdiff								
	Enduction 5600 rpm								

	Promoteur pyrox		
	Exposition		
	Développement	90 sec	
	Barrel 150W / O2 : 42%	60 sec	3h:00'
35	Décapage OxydeBuffer HF		
	630 A/min		
	Buffer HF	6' 30"	
	Rinçage H2O DI	10'	
36	Décapage résine acide nitrique	0h:10'	